CHALMERS

Aerodynamic Design and Installation Effects of Automotive Electric Cooling Fans

DEBARSHEE GHOSH

Department of Mechanics and Maritime Sciences
CHALMERS UNIVERSITY OF TECHNOLOGY
Gothenburg, Sweden 2023

Thesis for the degree of Licentiate of Engineering

Aerodynamic Design and Installation Effects of Automotive Electric Cooling Fans

Debarshee Ghosh

Department of Mechanics and Maritime Sciences
CHALMERS UNIVERSITY OF TECHNOLOGY
Göteborg, Sweden 2023

Aerodynamic Design and Installation Effects of Automotive Electric Cooling Fans
Debarshee Ghosh

© Debarshee Ghosh, 2023.

Licentiatavhandlingar vid Chalmers tekniska högskola
Technical report No. 2023:08

Department of Mechanics and Maritime Sciences
Chalmers University of Technology
SE–412 96 Göteborg, Sweden
Telephone + 46 (0) 31 – 772 1000

Chalmers Reproservice
Göteborg, Sweden 2023

To my family and Nikita.

Abstract

Aerodynamic Design and Installation Effects of Automotive Electric Cooling Fans
DEBARSHEE GHOSH
Department of Mechanics and Maritime Sciences
Division of Fluid Dynamics
Chalmers University of Technology

Electric cooling fans play a crucial role in automotive thermal management. They generate the airflow required for heat rejection from the expended coolant circulating within the heat exchanger. This thesis focuses on the aerodynamic design and installation effects of electric cooling fans or "E-fans". E-fans are low-pressure axial fans powered by individual electric motors due to the absence of an internal combustion engine in electric vehicles. These E-fans are often packaged very tightly due to the limited space in the underhood region. Additionally, they are often subjected to non-uniform inflow conditions as they are placed downstream of other components in the underhood region.

This thesis details the design process of low-pressure axial fans with low-solidity blades using the Blade Element Momentum (BEM) method. The design process takes into consideration the cooling system requirements. Three-dimensional, steady-state, Reynolds-Averaged Navier Stokes (RANS) simulations are performed on a single blade passage for a low-pressure axial fan rotor blade with a dimensional resemblance to the fans used for automotive cooling. The effect of an upstream blockage on the aerodynamic performance of the fan is investigated. A strong influence of the flow blockage on the aerodynamic performance is observed. A decrease in efficiency, an earlier onset of stall, and peak efficiency at lower volume rates is observed for increasing blockage of the fan face. Furthermore, the effect of installing two low-pressure axial fans in parallel on the aerodynamic performance of the fans is investigated. A circumferential non-uniformity in the flow which varies in space and time is observed at the fan inlet. However, this non-uniformity does not propagate down to the rotor blade and affect its performance. Consequently, no significant differences are observed in the operating condition of each of the fans in the two-fan installation in comparison to a single fan. This is considered as a positive outcome for vehicle manufacturers using similar multi-fan setups, where cooling fans are placed in parallel and in close proximity to one another.

Keywords: automotive thermal management, electric cooling fans, low-pressure axial fans, upstream blockage, fans in parallel, Blade Element Momentum (BEM), CFD simulations.

Acknowledgments

This research was performed at the Division of Fluid Dynamics, Department of Mechanics and Maritime Sciences at Chalmers University of Technology from August 2020 to May 2023. I would like to thank all the collaborators of this project; Chalmers University of Technology, Volvo Group Technology, Volvo Car Corporation, and the Swedish Energy Agency, without whom this work would be impossible.

I express my deepest gratitude to Professor Niklas Andersson and Associate Professor Sassan Etemad, for choosing me to participate in this project and allowing me to pursue my Ph.D. To Professor Niklas Andersson for always taking the time to hear me out, being my sounding board, and teaching me to trust the process, which I am sure has not been easy. To Associate Professor Sassan Etemad, for always being patient and believing in me, and allowing me to chart my course in the Ph.D., even if it meant not aligning with project goals occasionally.

I also extend a special thank you to Dr. Gonzalo Montero Villar for always being there to lend a helping hand, especially at the start of my Ph.D., and for being both a constant source of inspiration and a mentor.

I would also like to express my deepest gratitude to my parents, sister, and fiancée Nikita for their continued love and patience. A special thank you to my dear friend Julia, for always being just a door knock away. Last but in no way the least, I would like to thank all my colleagues at the Division of Fluid Dynamics for creating a pleasant working environment with a special shout out to Marily, Oliver, and Vinicius for making work feel a lot like home.

Debarshee Ghosh
Göteborg, April 2023

List of Publications

This thesis is based on the following appended papers:

Manuscript 1. Debarshee Ghosh, Niklas Andersson and Sassan Etemad. *Computational Fluid Dynamics Simulations of Aerodynamic Performance of Low-Pressure Axial Fans With Upstream Blockage.*

Manuscript 2. Debarshee Ghosh, Niklas Andersson, and Sassan Etemad. *Aerodynamic Analysis of Low-Pressure Axial Fans Installed in Parallel.*

Nomenclature

Acronyms

BEM	–	Blade Element Momentum
BEP	–	Best Efficiency Point
BEV	–	Battery Electric Vehicle
CFD	–	Computational Fluid Dynamics
DF	–	Diffusion Factor
EA	–	Evolutionary Algorithm
EV	–	Electric Vehicle
FAU	–	Friedrich-Alexander University
FCEV	–	Fuel Cell Electric Vehicle
HEV	–	Hybrid Electric Vehicle
HVAC	–	Heating Ventilation Air Conditioning
IC	–	Internal Combustion
IEA	–	International Energy Agency
LDA	–	Laser Doppler Anemometry
NACA	–	National Advisory Committee for Aeronautics
RANS	–	Reynolds-Averaged Navier Stokes
SST	–	Shear Stress Transport
URANS	–	Unsteady Reynolds-Averaged Navier Stokes

Latin Letters

a	–	speed of sound
c	–	absolute velocity
C_L	–	lift coefficient
C_D	–	drag coefficient
d_{fan}	–	fan diameter
d_{hub}	–	fan hub diameter
k	–	turbulent kinetic energy
l_c	–	chord length
$\dot{m}$	–	mass flowrate
p	–	pressure
P_{shaft}	–	input shaft power
Q	–	volume flowrate

s_b – blade spacing
s_{tip} – fan tip gap
T_{shaft} – input shaft torque
U – blade velocity
w – velocity in relative frame of reference
Y – specific work
z_b – blade count

Non Dimensional Number

Ma – Mach number
Re – Reynolds number

Greek Symbols

α – absolute flow angle
α – angle of attack
β – relative flow angle
γ – stagger angle
δ – specific diameter
ε – turbulence dissipation
ε – drag-to-lift ratio
η – efficiency
κ – hub-to-tip ratio
λ – power coefficient
ν – kinematic viscosity
ρ – fluid density
σ – specific speed
φ – flow coefficient
ψ – pressure coefficient
ω – rotational speed
ω – turbulence frequency
ξ – pressure loss coefficient

Subscripts

1 – rotor inlet station
2 – rotor outlet station
θ – circumferential component of velocity
t – total fluid property
ax – axial component of velocity
B – blade
CA – elemental blade cascade

d – dynamic component
m – meridional component of velocity
r – radial component of velocity
d – static component
ts – total-to-static fluid property
tt – total-to-total fluid property

Contents

Abstract **v**

Acknowledgments **vii**

List of Publications **ix**

Nomenclature **xi**

I Introductory Chapters 1

1 Introduction **3**
1.1 Background 3
1.2 Automotive thermal management system 4
1.3 Automotive cooling fans 6
1.4 The E-Fan project 7
1.5 Thesis outline and scope 9

2 Low Pressure Axial Fans **11**
2.1 Turbomachine classification 11
2.2 Fan performance parameters 11
2.3 System level fan design 13
2.3.1 System requirement 14
2.3.2 Fan type selection 15

3 Low Pressure Axial Fan Blade Design **19**
3.1 Blade cascade 19
3.1.1 Blade segmentation 22
3.1.2 Choice of airfoil profile 23
3.2 Flow kinematics - Radial equilibrium 23
3.3 Blade element method 28
3.4 Geometry summary 30
3.5 Summary 30

4 Summary of papers **33**
4.1 Paper 1 . . . 33
4.1.1 Methodology . . . 33
4.1.2 Discussion . . . 34
4.1.3 Division of work . . . 34
4.2 Paper 2 . . . 35
4.2.1 Methodology . . . 35
4.2.2 Discussion . . . 35
4.2.3 Division of work . . . 36

5 Conclusion **37**
5.1 Concluding remarks . . . 37
5.2 Future work . . . 38

Bibliography **39**

II Appended Papers **45**

1 Computational Fluid Dynamics Simulations of Aerodynamic Performance of Low-Pressure Axial Fans With Upstream Blockage **47**

2 Aerodynamic Analysis of Low-Pressure Axial Fans Installed in Parallel **63**

Part I

Introductory Chapters

Chapter 1

Introduction

1.1 Background

Transportation activities accounted for 23% of the total global greenhouse gas emissions in 2022, according to the International Energy Agency (IEA). However, over the past decade, the automotive industry, like several others, has made a concerted effort to reduce its carbon footprint through various measures to comply with the Paris Climate Agreement [1]. The automotive industry has taken significant steps towards reducing its contribution to greenhouse gases by embracing electric mobility as the future of road transport. Most large automotive manufacturers are rapidly transitioning toward electric propulsion through Hybrid Electric Vehicles (HEV), Battery Electric Vehicles (BEV), and Fuel Cell Electric Vehicles (FCEV).

Lithium-ion battery packs power the current generation of Electric Vehicles (EVs), minimizing the use of internal combustion (IC) engines and, by extension, the use of fossil fuels. EVs offer several advantages, such as the delivery of instant maximum torque, reduced noise, lower maintenance, and reduced environmental impact. As of 2021, IEA estimated 16.5 million on-road EVs, as shown in Fig. 1.1. The number of EVs in use is expected to reach 125 million by 2030 due to the growing customer demand and acceptance. However, heavy-duty EVs like buses and trucks are still in their nascent stages of customer adoption. In 2021, the global electric bus and heavy-duty truck stock accounted for about 4% and 0.1% of the global fleet, respectively.

The primary inhibition towards EV adoption among customers continues to be the lower driving range compared to their IC powered counterparts, especially for heavy-duty vehicles. IEA records the current median driving range of EVs on a single charge to be around 350km, about 50% of the median range of current gas powered vehicles on a full tank of fuel [2].

Increasing driving range typically requires larger batteries with higher power output capacity, which results in higher heat output. This brings into focus the thermal management system used for cooling the tightly packed underhood region. To ensure the continuing upward trend of driving range of EVs, the thermal management system must be developed simultaneously with the battery packs.

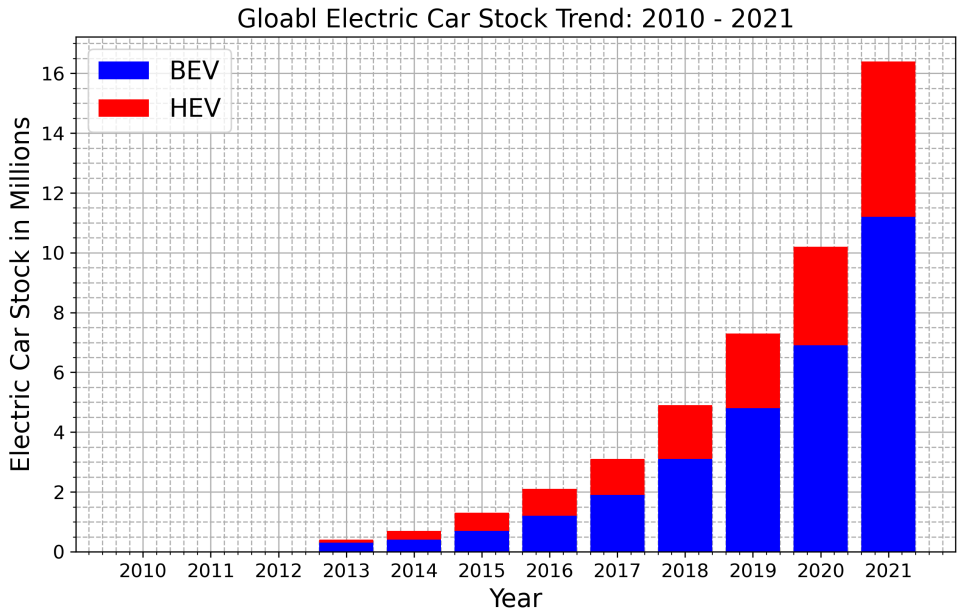

Figure 1.1: Global electric car stock trend from 2010-2021

1.2 Automotive thermal management system

Lithium-ion is the preferred choice of cell chemistry for electric propulsion due to its high specific energy, high energy density, long life cycle, and minimal memory effects. Lithium-ion batteries have twice the specific energy and energy density compared to nickel–metal hydride (NiMH) batteries, which dominated the HEV market in the early 2010s [3–6]. Multiple lithium-ion cells are combined to form a battery pack. In the absence of the IC engine, the battery pack is the primary heat source in EVs. Internal electrochemical reactions and resistance heating are the primary causes of the heat generated by the battery pack.

A lithium-ion battery pack's performance and durability is limited by its operating temperature. Several studies have accounted for the effect of high operating temperatures on the reduced performance and life of lithium-ion batteries [7–9]. Lithium-ion batteries have an ideal operating temperature window between $15°C$ and $40°C$. Additionally, the temperature variation between different cells of the battery pack is ideally to be limited below $5°C$ to ensure an optimal balance between durability and performance [10–12]. These requirements are tough to achieve under aggressive drive cycles, fast battery charging, and high ambient temperature conditions. The thermal management system also serves other functions, such as brake-power cooling during downhill braking, electric-circuit cooling, cabin temperature control, and ventilation of the underhood region to expel hazardous gases. An ideal thermal management system should maintain the battery pack at the optimum average temperature for all vehicle operating conditions, with only minor temperature variations between the cells of the battery pack.

There are currently several cooling solutions to meet the cooling requirements

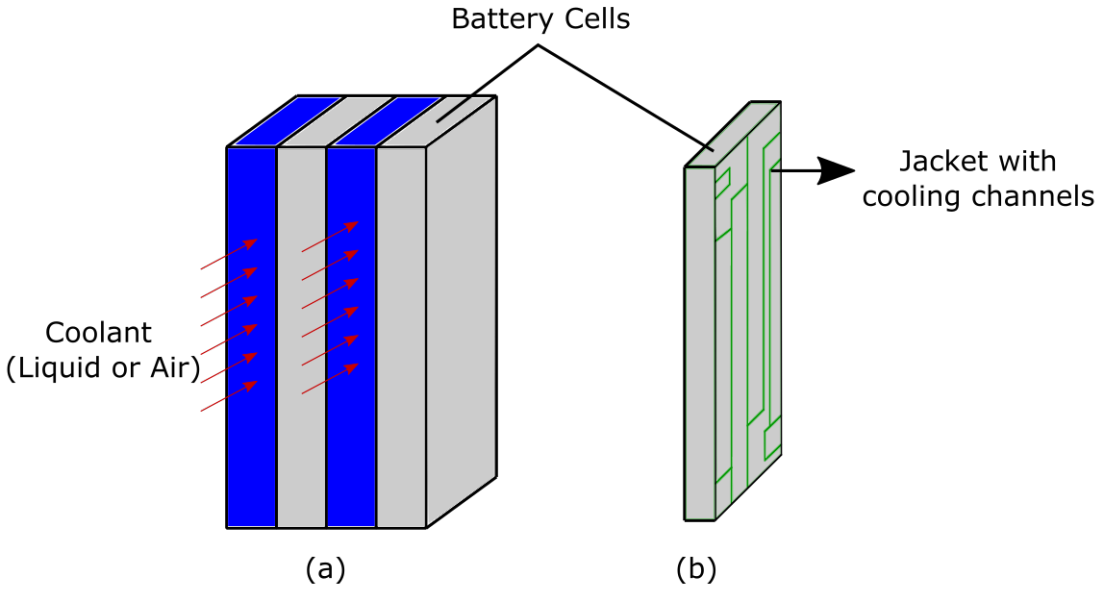

Figure 1.2: Battery Pack Cooling: (a) Direct cooling with air or liquid (b) Indirect cooling with coolant jacket mounted on battery cell.

imposed by the battery pack and other peripheral underhood components. Thermal management systems may use air, liquid, phase-change material or a combination as the heat sink for heat rejection from the battery pack. The current cooling solutions can be broadly classified into two categories; direct and indirect cooling. If the coolant comes into direct contact with the battery cell surface, the method is labeled as a direct cooling method. A schematic of a typical battery pack with different cooling solutions is illustrated in Fig. 1.2.

Ambient air is forced through the gap between two cells in a battery pack for direct air cooling. The airflow required for forced-convective cooling is generated as a result of the motion of the vehicle at high-to-medium speeds and through cooling fans. Direct air-cooling has the advantage of no-added weight. However, since this method employs cooling fans, which draw power from the battery itself, the parasitic power of the cooling package increases. Direct air cooling comes with the additional disadvantage of dependence on ambient temperature. The extent of heat rejection depends on the temperature difference between the source and the sink. At high ambient temperatures, the temperature difference between the battery pack and the ambient air reduces, and therefore the cooling ability of the air decreases. The cooling performance in such scenarios is addressed by increasing the surface area of the battery by adding fins, and is referred to as indirect air-cooling. [13]. However, the addition of fins comes with a weight penalty. Alternatively, the cooling performance may also be improved by increasing the velocity of the air passing over the battery pack surface. This requires the cooling fans to be operated at higher rotational speed or non-optimal operating conditions away from their peak efficiency point,

increasing the parasitic power of the cooling package. Direct air cooling, however, was successfully employed for cooling the early generation of HEVs [4–6].

A coolant is forced through the gap between the two cells in a battery pack for direct liquid cooling [12]. A dielectric coolant has to be used to prevent any electrical short circuits of the battery cell. Compared to the direct air-cooling method, additional components such as pumps, circulation channels, and heat exchangers are required in addition to cooling fans. Once the coolant absorbs the heat from the battery pack, it is circulated through the heat exchanger, where it is cooled through forced convection by the airflow generated by the cooling fans. Direct liquid cooling has the distinct advantage of being able to use coolants with thermal conductivity significantly greater than air. For indirect liquid cooling, a jacket with small channels for the coolant to circulate through is mounted over each battery cell, see Fig. 1.2. Indirect-liquid cooling allows greater control over the battery cell's surface temperature by appropriately positioning the channels on the jacket. Additionally, indirect liquid cooling allows for greater freedom in the choice of coolant, as it does not come into direct contact with the battery pack and therefore eliminates the need to use a coolant of dielectric nature [13]. However, this method too requires ancillary components like a pump, heat exchangers, and cooling fans like direct liquid cooling.

A comparative study between the different cooling methods performed by Chen et al. [14], concludes that direct air-cooling accounts for the highest parasitic power, direct liquid cooling offers the best cooling performance both in terms of peak temperatures of the battery and the temperature variation between cells of the battery pack, and indirect liquid cooling achieves slightly worse performance compared to direct cooling but is the more practical industrial solution.

1.3 Automotive cooling fans

A common factor across all cooling solutions presented in Sec. 1.2 is cooling by the airflow generated by cooling fans, either directly or indirectly. In the direct approach, the air is forced directly over the battery surface, and in the indirect cooling approach, the airflow is used to reject heat from the expended coolant in the heat exchangers. Since the specific heat and thermal conductivity of air is much lower than the coolant (1/10 and 1/4, respectively), forced convective cooling by air is the limitation in the heat rejection process. Hence, increasing the airflow is decisive for the cooling performance. Consequently, the cooling fan is the limiting factor and key to meeting the cooling requirements.

The airflow required for the heat rejection from the heat exchanger to the ambient air is generated by the cooling fans. The dimensions and positioning of the cooling fans are dictated by the space available in the underhood region, the shape of the heat exchanger, and the cooling requirements. Additionally, due to the limited space in the underhood region, these fans are often placed downstream of other components, causing them to ingest non-uniform flow. In vehicles powered by IC engines, cooling fans are mounted onto and powered by the crankshaft. However, since EVs do not

have a crankshaft, the cooling fans are instead powered by electric motors housed within their hub, and are therefore referred to as electric fans or "E-Fans".

The cooling requirement of the vehicle at different operating conditions dictates the mass flowrate of air to be ingested by the cooling fan. The required mass flowrate of air may be achieved by a single large diameter fan or multiple fans of smaller diameters arranged in parallel. Fans arranged in parallel have their respective rotational axes parallel to one another and are placed in identical axial positions. N fans arranged in parallel will deliver N times the mass flowrate of air compared to a single fan of the same diameter.

According to the fan laws, the fan performance scales with the fan diameter to the power of five (Head*Volumetric flow $\propto d_{fan}^5$) [15, 16], i.e., only a 15% increase in the fan diameter would double the performance and improve the efficiency. However, due to limited space, most manufacturers use several small diameter fans arranged in parallel instead of a single large diameter fan. This is especially true for passenger car manufacturers. However, multiple small diameter fans arranged in parallel offer several advantages over a single large diameter fan. Each fan in the parallel setup can be operated individually depending on the cooling requirement, consequently allowing each fan to be operated as close as possible to its maximum efficiency point. Using a parallel fan setup also allows for better homogeneous mixing of the flow downstream of the fans.

1.4 The E-Fan project

The thermal management requirements of IC engine powered vehicles heavily influence automotive cooling fan development. The existing "off-the-shelf" cooling fans usually perform poorly for commercial EVs. Thus, a new generation of cooling fans that cater to the thermal requirements of the current generation of EVs is required. Additionally, most existing automotive cooling fans are developed and tested in fan test rigs and not in the underhood environment. Once installed in the vehicle, the cooling fans become exposed to several disturbances that negatively influence its performance, efficiency, and noise.

A summary of the scientific work concerning cooling and ventilation fans is presented here to establish the current state of research in this field. Here it is important to note that automotive cooling fans, in most cases, are low-pressure axial fans. Low-pressure axial fans are ideal for delivering high volume flowrate of air at minimal pressure rise, making them ideal choices for cooling and ventilation applications.

Castegnaro.S. [17] provides a comprehensive review of the historical design philosophies of low-pressure axial fans. Classical aerodynamic design methodologies relied on empirical data and simplified one-dimensional cascade analysis [18–20].

Much of the current scientific work, both numerical and experimental, concerning low-pressure axial fans focus on blade design. The effect of blade loading distribution on aerodynamic performance is of significant interest. Radius dependent blade loading distribution allows for better utilization of the rotor at higher spans, allowing for lower loading at the rotor hub. This reduces the possibility of hub separation and

allows for rotor blade designs with high-specific performance [21]. Three-dimensional rotor blade angles, namely the circumferential skew, sweep, and dihedral angle, are frequently investigated design parameters to improve rotor aerodynamic efficiency [22–25].

More recently, the desire to explore the entire design space has led to optimization studies using Evolutionary Algorithms (EA) in conjunction with CFD to optimize the aerodynamic efficiency of the rotor blade by varying blade design parameters, such as the hub-to-tip diameter ratio (κ), the radial distribution of the blade sweep angle, the stagger angle, the chord length, and the stacking line [26, 27].

Small hub-to-tip diameter ratio fans are often desirable for automotive cooling. This is especially true for cases where the heat exchanger is placed downstream to the fan. A small hub-to-tip diameter ratio reduces the flow blockage to the heat exchanger when the fan is standing still and the airflow required for cooling is achieved through vehicle motion at medium to high speeds. Wang and Kruyt [28] investigated the aerodynamic performance of a low-pressure axial fan with very small hub-to-tip diameter ratio ($\kappa = 0.14$), numerically. Masi et al. [24] investigated three fans with medium hub-to-tip diameter ratios ($\kappa < 0.5$). Both aerodynamic and aero-acoustic experimental investigations on a ducted rotor-only low-pressure axial fan with medium hub-to-tip diameter ratio ($\kappa = 0.5$) was performed by Zenger et al. [29–31]. The numerical validation of the experiments conducted by Zenger et al. [29–31] was performed by Schoder et al. [32]. Several scientific works have investigated the effect of the tip-clearance, a known source of losses in any turbomachinery, for low-pressure axial fans [33, 34].

Although low-pressure axial fans have been studied extensively, the amount of reported scientific work studying fans installed in parallel is very limited. Most scientific work for parallel fan setups has been performed for either underground mining fans [35, 36], or fans used in Heating, Ventilation, and Air Conditioning (HVAC) systems [37]. HVAC fans are mostly centrifugal fans and therefore are irrelevant to this work. Underground mining fans are axial fans but have no dimensional or operational resemblance to automotive cooling fans.

Here, it is concluded that significant scientific literature exists around the rotor design of low-pressure axial fans operating in stand-alone mode while ingesting uniform flow. However, limited work exists concerning the aerodynamic performance of low-pressure axial cooling fans when operating in the tightly packed underhood region. The goal of the E-Fan project is to bridge this gap and build a better understanding of the aerodynamic performance of cooling fans when installed in the underhood region. This entails understanding the aerodynamic performance of cooling fans when subjected to generic upstream disturbances, downstream blockage, and interaction between fans when installed in a parallel setup. Ultimately, this project aims to develop cooling fans which are specifically designed to cater to the unique thermal requirements of the current and future generation of EVs.

1.5 Thesis outline and scope

This work focuses on the design and installation effects of low-pressure axial fans in automotive cooling systems. The introductory chapters focus on the design of low-pressure axial fans, as it is the intention of the author of this work to design a low-pressure axial fan to use in the latter half of the project. Chapter 2, identifies the basic design parameters required for fan design, which is obtained from the cooling system requirements. Chapter 3, utilizes these basic design parameters and focuses on the blade design. The basic blade design methodology for low-pressure axial fans with low-solidity blades using the Blade Element Momentum (BEM) method is described in Chapter 3. However, the design of the fan blades using the BEM method is limited by the assumption of uniform flow at the rotor inlet. The aerodynamic performance of cooling fans when installed in the underhood region is investigated in the appended papers. Paper 1 investigates the effect of upstream blockage on the aerodynamic performance of a low-pressure axial fan with dimensional resemblance to automotive cooling fans. These automotive cooling fans are often installed in parallel in close proximity to one another as a part of the cooling package. Paper 2 investigates the aerodynamic performance of two fans installed in parallel. Ultimately, this work aims to develop a better understanding of both the fan design process and installation effects of low-pressure axial fans when installed in the tightly packed underhood region.

Chapter 2

Low Pressure Axial Fans

2.1 Turbomachine classification

Turbomachines transfer energy to or from a continuously moving fluid through the dynamic action of moving blade rows by changing the stagnation enthalpy of the fluid. They are broadly classified as turbines or pumping devices, depending on the direction of energy transfer. Pumping devices absorb power and increase the pressure or head of the fluid. Alternatively, a turbine produces energy by expanding the fluid to a lower pressure or head. Turbomachines are further classified based on the flow direction at the rotor outlet. If the flow direction at the rotor outlet is primarily parallel to its rotational axis, it is classified as an axial-flow machine. Alternatively, if the flow direction at the rotor outlet is predominantly perpendicular to the rotational axis, it is classified as a radial-flow machine. Finally, if the flow direction at the rotor outlet has significant axial and radial components, it is classified as a mixed-flow machine. Based on the operation regime, turbomachines are classified as compressible and incompressible machines. Compressible effects should be accounted for in flows where density changes are significant (typically if $\Delta\rho/\rho > 5\%$), i.e., in addition to flows which have Mach number greater than 0.3, the compressible effects also need to be accounted for flows with low velocity but significant pressure fluctuations. The classification of turbomachines is illustrated in Fig. 2.1. This thesis focuses on low-pressure axial fans, which are essentially incompressible axial pumping devices.

2.2 Fan performance parameters

The operating point of a fan is quantified by its rotational speed (ω in rad/s) and ingested mass flowrate ($\dot{m}$ in kg/s). For a fan operating in the incompressible flow regime, the volume flowrate (Q in m^3/s) is the more appropriate quantity to measure the flow ingested by the fan, as the density (ρ in kg/m^3) remains constant.

At a given operating point, the increase in the flow pressure is quantified by the total-to-total pressure rise (p_{tt} in Pa), calculated as the difference in the mass-flow averaged total pressure at the fan exit ($p_{t,exit}$) and the fan inlet ($p_{t,inlet}$), according to Eq. (2.1). The total pressure is the sum of the dynamic and static pressure. The

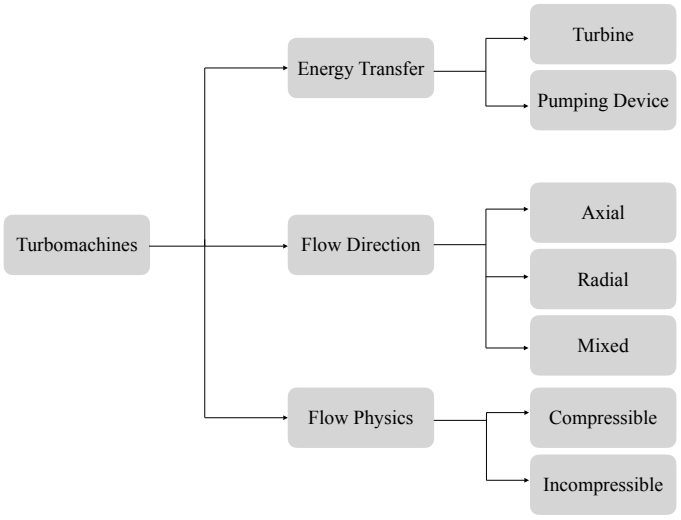

Figure 2.1: Turbomachinery Classification

.

dynamic pressure (p_d) is calculated as ($\rho c^2/2$), where c is the velocity at the fan inlet (c_{inlet}) or at the fan outlet (c_{exit}).

However, when the fan is the last component of the plant and exhausts freely into atmospheric conditions such as a large room, the dynamic pressure of the jet exiting the fan constitutes a loss. Therefore the dynamic pressure at the fan outlet ($p_{d,exit}$) must not be accounted for in the effective pressure increase achieved by the fan. In this case, the effective pressure rise achieved by the fan is reported by eliminating the dynamic pressure at the exit. The total-to-static pressure rise (p_{ts} in Pa) is instead used to report the effective pressure increase, according to Eq. (2.1), where $p_{st,exit}$ is the area-averaged static pressure at the fan outlet and $p_{t,inlet}$, is the mass-flow averaged total pressure at the fan inlet.

$$p_{tt} = (p_{t,exit} - p_{t,inlet}) \quad ; \quad p_{ts} = (p_{st,exit} - p_{t,inlet}) \tag{2.1}$$

The power required by the fan to increase the flow pressure, is calculated as the product of the rotational speed of the fan (ω) and torque of the motor shaft (T_{shaft} in Nm) used to power the fan, according to Eq. (2.2).

$$P_{shaft} = \omega T_{shaft} \tag{2.2}$$

The corresponding efficiency of the fan is calculated according to Eq. (2.3). When the fan is exhausting into atmospheric conditions the efficiency is reported as the total-to-static efficiency (η_{ts}), and is calculated using the total-to-static pressure (p_{ts}). Ultimately, the aerodynamic performance of the fan at a given operating point is quantified by the fan pressure rise (p_{tt} or p_{ts}) and the fan efficiency (η_{tt} or η_{ts}).

$$\eta_{tt} = \frac{Q\ p_{tt}}{P_{shaft}} \quad ; \quad \eta_{ts} = \frac{Q\ p_{ts}}{P_{shaft}} \tag{2.3}$$

The regime of operation of a turbomachine is quantified by the Mach Number (Ma) and the Reynolds number (Re), calculated according to Eq. (2.4). Low-pressure

axial fans operate in the incompressible and turbulent flow-regime. For low viscosity flows at high speeds ($Re > 2 * 10^5$), the effects of Reynolds number on turbomachine performance is low [38]. This can be attributed to the formation of very thin and turbulent viscous boundary layers around the rotor blade surface, which have minimal effect on the global flow field.

$$Re = \frac{\Omega \, d_{fan}^2}{4\nu} \quad ; \quad Ma = \frac{\Omega \, d_{fan}}{2a} \tag{2.4}$$

Non-dimensional parameters are often used to quantify the operating point and aerodynamic performance of turbomachines. Non-dimensional numbers enable the comparison between geometrically similar turbomachines, different operating conditions, and comparison between experimental and numerical data. For a turbomachine operating in the incompressible flow regime, the non-dimensional numbers are expressed in terms of control variables (ω and Q), geometric variables (d_{fan}), and fluid flow properties (ρ). The three non-dimensional numbers of interest, are the flow coefficient (ϕ), the pressure coefficient (ψ), and the power coefficient (λ). Each non-dimensional number is expressed as a combination of the control variables, geometric variables and flow properties, in Eq. (2.5) [15, 16]. Here it is also important to note the difference in the definition of non-dimensional parameters in German and English literature. For this work and the appended papers, the German definition of the non-dimensional coefficients has been used [15, 39].

$$\varphi = \frac{8 \, Q}{\pi \omega d_{fan}^3} \quad ; \quad \psi = \frac{8 \, p}{\rho \omega^2 d_{fan}^2} \quad ; \quad \lambda = \frac{64 \, P_{shaft}}{\rho \omega^3 d_{fan}^5} \tag{2.5}$$

To determine the overall operating range of any given fan, a speed-line is constructed. In order to obtain a speed-line for a fan, as shown in Fig. 2.2, the volume flowrate of air ingested by the fan is changed while keeping the fan's rotational speed constant. The pressure and efficiency of the fan increase as the volume flowrate of air decreases until a specific point known as the Best Efficiency Point (BEP). At the BEP, the fan operates at its peak aerodynamic efficiency. If the fan operates at a volume flowrate greater than the BEP, it is considered to be operating in overload conditions. Alternatively, if the fan operates at a volume flowrate smaller than the BEP, it is said to be operating at part-load condition. When the volume flowrate of air being ingested by the fan is smaller than the point at which stall occurs, see Fig. 2.2, large-scale separations occur on the blade surface, which results in a sudden decrease in fan efficiency. It is not desirable to operate the fan in the stall region.

2.3 System level fan design

This section outlines the details of the basic design parameters obtained from the cooling system requirements.

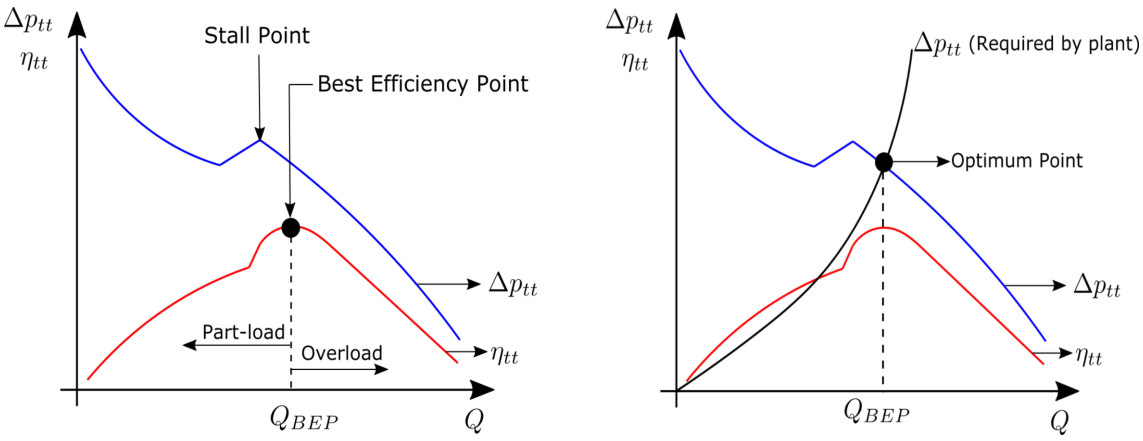

Figure 2.2: Aerodynamic characteristic curve for a fixed rotational speed of the fan (**left**) with characteristic curve for the cooling system included (**right**), adapted from [15].

2.3.1 System requirement

The fan design process begins with identifying the system requirements it must fulfill. For an automotive cooling system, this entails:

- Determining the volume flowrate (Q) of air required for rejecting heat from the expended coolant in the heat exchanger. The cooling requirements of the various components of the underhood region at different vehicle operating conditions determine the required volume flowrate of air.

- Determining the maximum fan diameter (d_{fan}) that can be used. This is motivated by the size and shape of the heat exchanger. The system choice of using a single-fan or a multi-fan setup also plays a role when choosing the maximum dimension of the fan. However, as previously mentioned in Sec. 1.3, multi-fans are the preferred choice due to their modular setup.

- Determining the total-to-total pressure increase ($\Delta p_{tt,req}$) the fan must achieve for the specified volume flowrate. The total-to-total pressure increase required to be achieved by the fan is motivated by the vehicle operating condition, as it determines the dynamic component of the flow entering the underhood region.

Figure. 2.3 illustrates an arbitrary fan, where station-1 and station-2 represent the boundaries of the control surface around the fan. Flow enters through station-1 and leaves through station-2. Between station-1 and station-2, the total pressure of the flow must be increased by a value $\Delta p_{tt,req}$, according to Eq. (2.6). The total pressure losses that occur in the system, due to ancillary components needs to be compensated for by the fan and therefore is included in the total pressure rise that the fan must achieve. Ultimately, the fan is designed for a total pressure rise equal to $\Delta p_{tt,req}$. The pressure losses, due to ancillary components such as casing, diffusor, and ducts are calculated according to Eq. (2.7). The pressure loss coefficient (ξ) for the each ancillary component may be obtained from common literature [40].

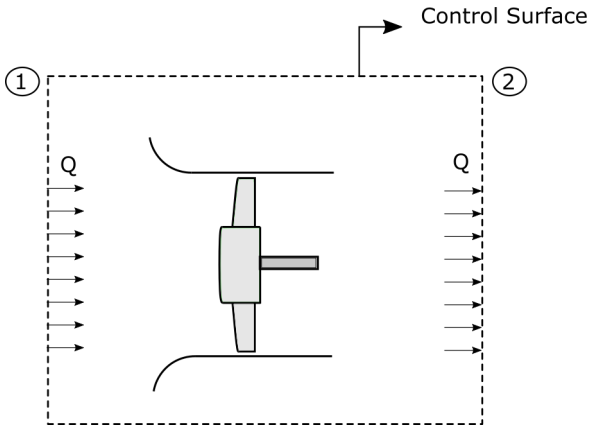

Figure 2.3: Schematic of a fan placed upstream of heat exchanger, within control volume

.

The total-to-total pressure increase that the fan is required to achieve can also be plot as a characteristic curve, as illustrated in Fig. 2.2. Since all velocities in Eq. (2.6) and Eq. (2.7), are proportional to the volume flowrate, the characteristic curve for the total-to-total pressure increase that the fan is required to achieve, is best approximated as a quadratic curve, see Fig. 2.2. Ideally a fan must be designed such that its peak efficiency point, coincides with the most likely to occur vehicle cooling requirement cycle, while still being sufficiently robust to handle off-design conditions.

$$\Delta p_{tt,req} = (p_2 - p_1) + \frac{\rho}{2}(c_2^2 - c_1^2) + \Sigma \Delta p_{loss} \tag{2.6}$$

$$\Delta p_{loss} = \xi \left(\frac{\rho c^2}{2} \right) \tag{2.7}$$

2.3.2 Fan type selection

Once the requirements for the cooling system are known (Q, d_{fan}, $\Delta p_{tt,req}$, and ρ), a choice of the type of fan to be used is made. To do this, two additional non-dimensional parameters, namely the specific speed (σ) and the specific diameter (δ) are calculated according to Eq. (2.8) and Eq. (2.9), respectively. In Eq. (2.8), n is the rotational speed of the fan in rotations per second (rps). The design choice for the rotational speed of the fan is made based on the available motor and motor control unit. Again here, a difference exists in the definition of specific speed and specific diameter between German and English literature. The definitions from German literature are used for this work and the appended papers.

$$\sigma = \frac{(2\pi^2)^{\frac{1}{4}}\ n\ \rho^{\frac{3}{4}}\ Q^{\frac{1}{2}}}{\psi_{tt}^{\frac{3}{4}}} = \phi^{\frac{1}{2}}\ \psi_{tt}^{-\frac{3}{4}} \tag{2.8}$$

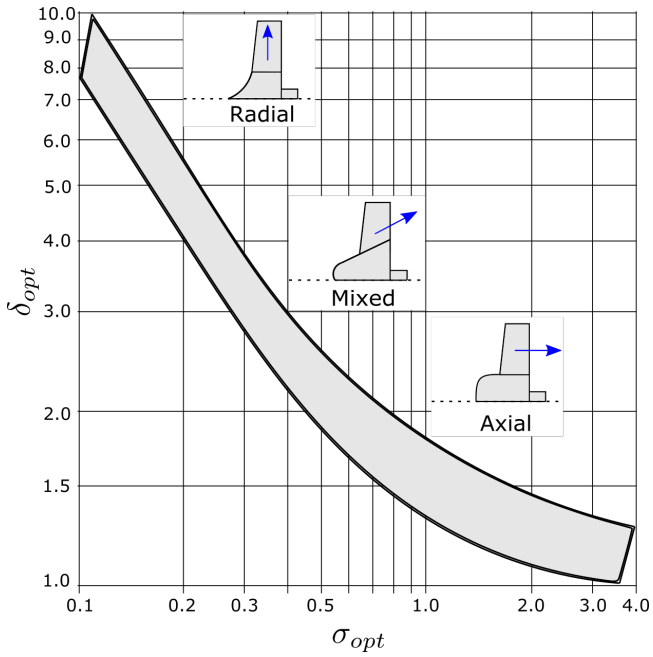

Figure 2.4: Cordier Diagram, adapted from [41]

.

$$\delta = \frac{d_{fan}\ \psi_{tt}^{\frac{1}{4}}}{(8\pi^2)^{\frac{1}{4}}\ \rho^{\frac{1}{4}}\ Q^{\frac{1}{2}}} = \phi^{-\frac{1}{2}}\ \psi_{tt}^{\frac{1}{4}} \tag{2.9}$$

Figure. 2.4 illustrates the Cordier diagram [41], an essential tool used to select the optimal fan design for a given operating range by relating specific speed and specific diameter. The Cordier diagram was derived empirically from measurement data. The specific speed and diameter were calculated for the operating point with the highest efficiency for different rotor types. These points were transferred into the Cordier diagram and were found to lie within a certain band. This band represents the best possible rotor configurations for a given specific speed and diameter. This optimal band is illustrated as the gray-colored band in Fig. 2.4.

As an example to illustrate the use of the Cordier diagram for fan selection, an axial fan with an optimal specific speed $\sigma_{opt} = 1.54$ is chosen. Similarly, an optimal specific speed of $\sigma_{opt} = 0.41$ is chosen for the radial fan. The diameter for the fans are chosen such that both the axial and radial fans operate within the optimal band in the Cordier diagram in Fig. 2.4.

Figure. 2.5 illustrates the speed lines for the axial and radial machine for the given specific speed and diameter (adapted from [15]). The radial machine achieves a higher total-to-total pressure rise (Ψ_{tt}) for a given volumetric flowrate compared to an axial fan. However, the radial machine has a much smaller range of operation than the axial machine, i.e., the range of flow coefficient (ϕ), it can operate over without stalling. It is also noted that in Fig. 2.5, the peak total-to-total efficiency ($\eta_{tt,max}$) for the axial fan is achieved at a higher flow-coefficient for an axial fan compared to a radial fan. In general, axial fans are high specific speed ($\sigma_{opt} > 0.6$) and low-specific diameter devices ($\delta_{opt} < 0.3$). For automotive cooling systems, the volume flowrate

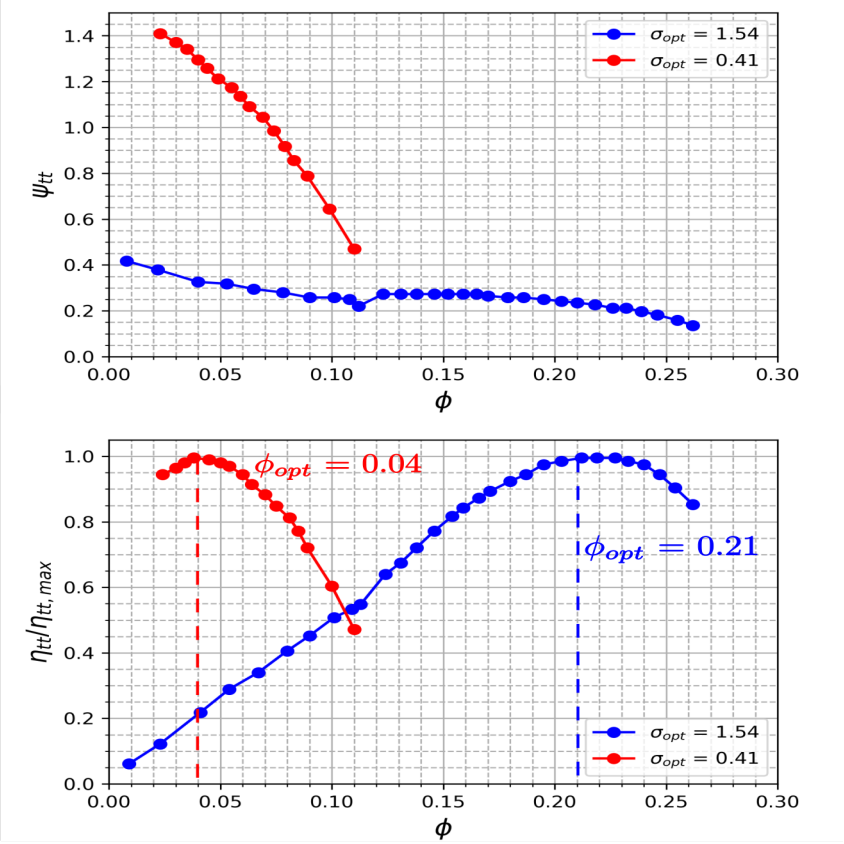

Figure 2.5: Comparison between aerodynamic performance characteristic of an axial fan ($\sigma_{opt} = 1.54$) and radial fan ($\sigma_{opt} = 0.41$), adapted from [15].

of air generated by the low-pressure axial fan is of significant importance. Due to the large range of operating conditions within which the vehicles must operate, low-pressure axial fans, which operate over large range of flow coefficients without stalling, is the ideal choice. Ultimately from the requirements imposed by the cooling system, the choice of motor and motor control unit, the following basic design parameters for a low-pressure axial fan are obtained:

- The volume flowrate of air to be delivered by the fan (Q)
- The total-to-total pressure rise that the fan must achieve ($\Delta p_{tt,req}$)
- The density of the flow (ρ)
- The rotational speed of the fan (ω)
- The maximum diameter of the fan (d_{fan})

Chapter 3

Low Pressure Axial Fan Blade Design

Once the choice of fan has been made according to the steps outlined in Ch. 2, the next step is to design the blade to achieve the system requirements. This chapter outlines the basic design philosophy implemented for the design of low-pressure axial fan blades with low-solidity using the Blade Element Momentum (BEM) method.

3.1 Blade cascade

Work is done on the fluid by the rotating blades by changing the stagnation enthalpy of the flow. The blade design parameters are the total specific blade work ($Y_{t,B}$), and the mass or volume flowrate of air through all blade channels ($\dot{m}_B$ or Q_B).

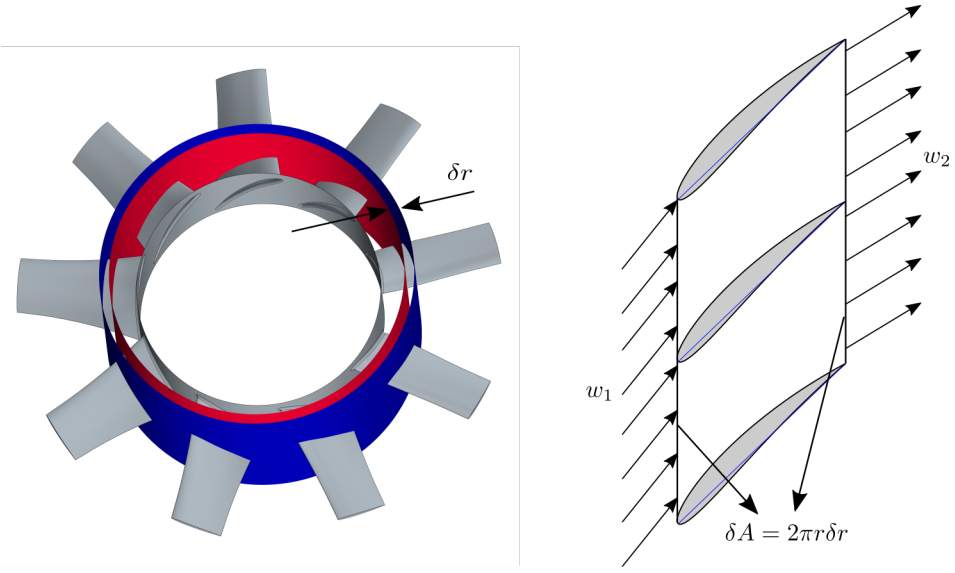

Figure 3.1: A rotor segmented using co-axial cylindrical rings, separated by a radial distance (δr) (**left**). The resulting elemental blade cascade with multiple blade elements and inlet are δA (**right**).

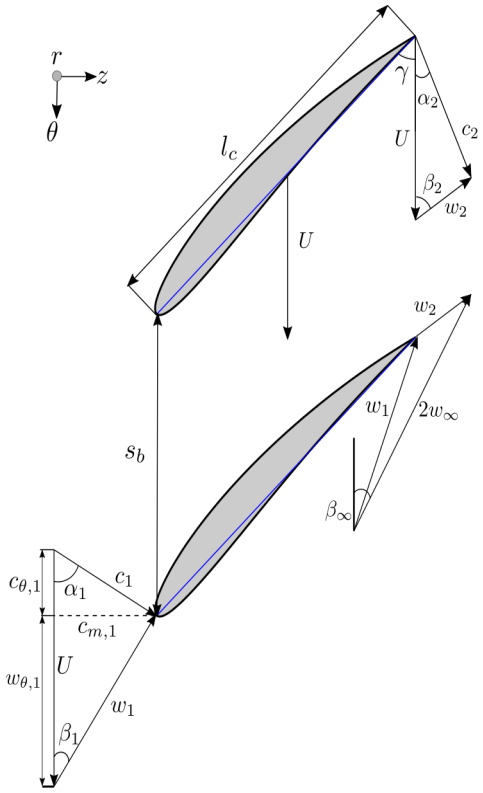

Figure 3.2: Inlet (subscript **1**) and outlet (subscript **2**) velocity triangle for an axial fan, adapted from [15].

The total specific work performed by the blade on the fluid is calculated, according to Eq. (3.1). The total pressure rise achieved by the blades is denoted by $\Delta p_{t,B}$. The total pressure rise achieved by the fan (Δp_{tt}), must then be equal to the total-pressure rise desired for the system ($\Delta p_{tt,req}$).

$$Y_{t,B} = \left(\frac{\Delta p_{t,B}}{\rho} \right) \tag{3.1}$$

To calculate the total pressure rise achieved by the blade ($\Delta p_{t,B}$), two-dimensional cascade analysis is implemented [15, 16]. A cascade analysis is performed on an elemental blade cascade. Two coaxial rings separated by a radial distance, δr, as illustrated in Fig. 3.1 are considered to obtain an elemental blade cascade, with inlet and exit area $\delta A = 2\pi r \delta r$.

In Fig. 3.2, the inlet and outlet velocity triangle are illustrated for an elemental blade cascade. Again here it is noted that there is a difference from the notations used commonly in English literature. All velocity components denoted by c and angles denoted by α are with respect to the absolute frame of reference. All velocity components denoted by w and angles denoted by β are with respect to the rotational frame of reference. Both the absolute velocity and relative velocity are the vector sum

of their respective axial, radial and circumferential velocity components, according to Eq. 3.2.

$$\overrightarrow{c} = (\overrightarrow{c_{ax}} + \overrightarrow{c_{rad}} + \overrightarrow{c_{\theta}}) \quad ; \quad \overrightarrow{w} = (\overrightarrow{w_{ax}} + \overrightarrow{w_{rad}} + \overrightarrow{w_{\theta}}) \tag{3.2}$$

The meridional velocity is calculated as the vector sum of the axial and radial component of velocity, according to Eq. (3.3). For an axial fan, the meridional velocity component of the absolute velocity remains constant between rotor inlet and outlet, i.e., $c_{m,1} = c_{m,2}$. For a purely axial fan operating at the BEP, the radial velocity component both at rotor inlet and outlet should be zero, i.e., the meridional velocity component is equal to the axial velocity component.

$$\overrightarrow{c_m} = \overrightarrow{c_{ax}} + \overrightarrow{c_{rad}} \tag{3.3}$$

Since the blade velocity (U) by definition is only in the tangential direction, there is no change in the axial and radial velocity component when moving from the stationary frame of reference to the relative frame of reference, i.e., the meridional velocity component in the absolute and relative frame of reference are the same, see Eq. (3.4). The blade velocity (U) is calculated as the product of the rotational speed of the fan (ω) and the blade radius (r). The circumferential velocity component in the relative frame of reference is calculated as the difference in the blade velocity (U) and the absolute circumferential component (c_θ), i.e., $w_\theta = U - c_\theta$.

$$\overrightarrow{c_{ax}} = \overrightarrow{w_{ax}} \quad ; \quad \overrightarrow{c_{rad}} = \overrightarrow{w_{rad}} \quad ; \quad \overrightarrow{c_m} = \overrightarrow{w_m} \tag{3.4}$$

The absolute flow angle at the rotor inlet or outlet is calculated as the ratio of the meridional component and the circumferential component of velocity, according to Eq. (3.5).

$$\alpha = arctan\left(\frac{c_m}{c_\theta}\right) \quad ; \quad \beta = arctan\left(\frac{c_m}{U - c_\theta}\right) \tag{3.5}$$

As the fluid moves through the blade passage, the rotor performs work on the flow by turning the flow. Due to the flow being turned, the absolute flow angle at the rotor outlet is smaller than at the rotor inlet ($\alpha_1 > \alpha_2$), in Fig. 3.2. The absolute circumferential velocity component at the rotor outlet is greater in magnitude than at the rotor inlet, i.e., $c_{\theta_2} > c_{\theta_1}$ for any specified blade radius. As the flow moves through the blade passage the flow is slowed down and therefore, w_2 is smaller in magnitude compared to w_1. The vectorial mean (w_∞) of the relative velocity at the rotor inlet is introduced here and is calculated according to Eq. (3.6). The vectorial mean of the relative velocity at rotor inlet and outlet is used later in the design process in the BEM method in Sec. 3.3.

$$\overrightarrow{w}_\infty = \frac{1}{2}\left(\overrightarrow{w}_1 + \overrightarrow{w}_2\right) \tag{3.6}$$

$$w_\infty = \frac{1}{2}\sqrt{\left(u + \sqrt{w_2^2 - c_m^2}\right)^2 + 4c_m^2} \tag{3.7}$$

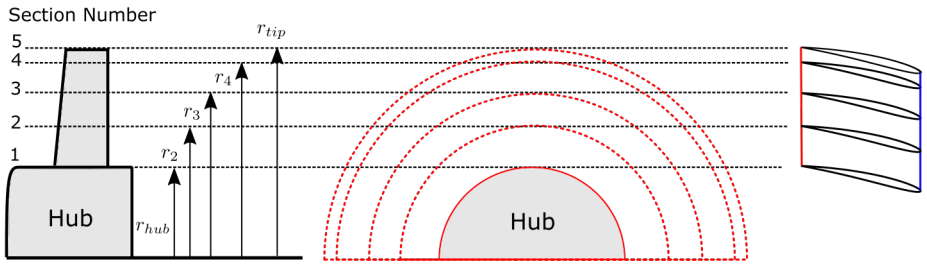

Figure 3.3: Segmentation of the blade annulus from rotor hub to tip, with equal area sections,adapted from [15]

$$\beta_\infty = tan^{-1}\left(\frac{2c_m}{u + \sqrt{w_2^2 - c_m^2}}\right) \tag{3.8}$$

From Euler's turbomachinery equation, the specific work done on the fluid by an elemental blade-cascade, is the product of the blade velocity (U) and the difference in the circumferential velocity components at rotor exit and rotor inlet, Eq. (3.9). Here the subscript CA, represents a single elemental blade cascade at a specific blade radius. The total specific work done by the entire blade is obtained by a summation over all elemental blade cascades, according to Eq. (3.10).

$$Y_{t,CA} = U(c_{\theta,2} - c_{\theta,1}) \quad and \quad \Delta p_{tt,CA} = \rho U(c_{\theta,2} - c_{\theta,1}) \tag{3.9}$$

$$Y_{t,B} = \frac{1}{Q_B}\sum_{all\ CA} Y_{t,CA}\ \delta Q_{CA} \tag{3.10}$$

3.1.1 Blade segmentation

The first step of the blade design process is the segmentation of the blade annulus into elemental blade cascades. The segmentation of the blade annulus may be performed in several ways. One such method is to segment the annular area between the rotor hub and tip, such that the through-flow area between successive co-axial blade segments have an equal area (δA), as illustrated in Fig. 3.3. The radius of each elemental blade cascade is then calculated according to Eq. (3.11). Here r_{tip} and r_{hub} are the radius of the rotor hub and tip respectively and n is the number of chosen blade segments. In this approach the first and last blade segment will always coincide with the rotor hub and rotor tip, respectively.

$$r_j = \sqrt{r_{hub}^2 + \frac{(j-1)(r_{tip}^2 - r_{hub}^2)}{n-1}} \quad ; \quad j = 1, 2, ...n \tag{3.11}$$

3.1.2 Choice of airfoil profile

Once the blade annular area has been segmented, a choice needs to be made regarding the airfoil profile to be used. Typically low-pressure axial fans have a low-blade count (z_b), high-circumferential blade spacing (s_b), and consequently have low-solidity blades [19, 23, 24, 26, 28]. Blade solidity is defined as the ratio of blade chord-length (l_c) to the blade spacing (s_b), according to Eq. (3.12). For low-pressure axial fans the blade solidity should be maintained below 0.7 for all blade considered blade segments, to ensure limited aerodynamic interaction from adjacent blades [15, 19].

$$\sigma = \left(\frac{l_c}{s_b}\right) \tag{3.12}$$

The four digit National Advisory Committee for Aeronautics (NACA) [42] airfoil series is a common choice for low-pressure axial fan blade design since these airfoil profiles allow for the individual control of the mean camber line and the thickness distribution around the same. This series of airfoils generate weakly cambered blades ($f/l_c < 0.1$), where f is the maximum camber. The choice of airfoil provides the airfoil polar curves, i.e., the lift coefficient (C_L) and the drag-to-lift ratio (ε) as a function of the angle of attack (α) and Reynolds Number (Re). The airfoil polar curves for an isolated NACA 4412 airfoil is illustrated in Fig. 3.4, for a range of Re numbers. The airfoil polar curves can be computed with the public domain code XFOIL by Drela [43].

It is observed that as Reynolds number increases the the lift coefficient curve converges. Similarly, the lift-to-drag ratio curves converge with increased Reynolds number. Typically it is recommended that the Reynolds number calculated using the blade chord length (l_c) as the reference dimension, be maintained above $1.5 * 10^5$ for all blade segments [15]. The chosen airfoil and its corresponding airfoil polar curves play a key role in the BEM method.

3.2 Flow kinematics - Radial equilibrium

As specified in Sec. 3.1, for a purely axial fan operating at the BEP, the radial velocity component should be zero at both the rotor inlet and outlet. Thus reducing the flow to only two-velocity components, i.e., axial and circumferential velocity components. To ensure, this two-dimensional flow, the sum total of the radial forces acting on a fluid element passing through the rotor must be zero. A zero radial velocity component ensures that the streamlines are located on co-axial cylindrical surfaces. Ideally, this condition of zero radial component of flow, must be satisfied everywhere inside the blade passage. However, it is sufficient to ensure that this condition is satisfied just upstream and downstream of the rotor. A plane immediately downstream of the rotor is considered, in Fig. 3.5. A small fluid element of elemental mass (dm) on a plane downstream of the rotor has pressure and centrifugal forces acting on it in the radial direction, where $dm = \rho dAdr$. The angular velocity experienced by the elemental mass ($\omega^{'}$), is calculated as ($c_{\theta,2}/r$), which leads to the elemental mass experiencing a centrifugal force equal to $r\omega^{'2}dm$.

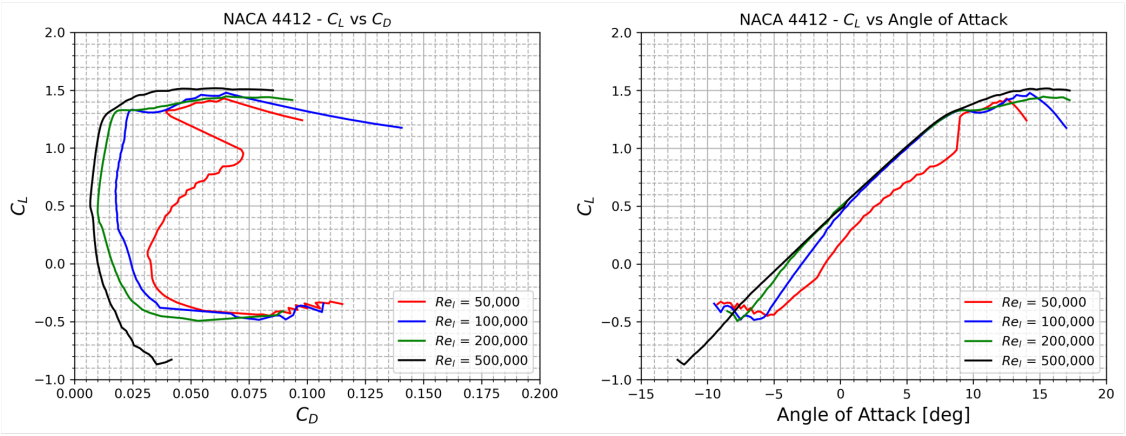

Figure 3.4: Polar curves for the NACA 4412 isolated airfoil at different Reynolds number: C_L vs C_D (**left**) and C_L vs α (**right**).

To achieve radial equilibrium the sum of the forces acting on the element mass must be zero, according to Eq. (3.13). Replacing values of dm and $\omega^{'}$ in Eq. (3.13), yields Eq. (3.14). Here it is important to note that both the pressure (p_2) and the circumferential velocity component at the rotor downstream plane ($c_{\theta,2}$) are functions of the blade radius.

$$p_2 dA - (p_2 + dp_2)dA + r\omega^2 dm = 0 \tag{3.13}$$

$$\frac{dp_2}{dr} = \rho \frac{c_{\theta,2}^2}{r} \tag{3.14}$$

The total pressure on the rotor downstream plane ($p_{t,2}$) is defined as the sum of the static and dynamic component, according to Eq. (3.15). Differentiating Eq. (3.15) with respect to r, yields Eq. (3.16). Substituting (dp_2/dr), from Eq. (3.14) into Eq. (3.16), yields Eq. (3.17). The first two terms of Eq. (3.17), combine according to the differentiation product rule to yield Eq. (3.18).

$$p_{t,2} = p_2 + \left(\frac{\rho c^2}{2}\right) = p_2 + \frac{\rho}{2}(c_{\theta,2}^2 + c_{m,2}^2) \tag{3.15}$$

$$\frac{dp_{t,2}}{dr} = \frac{dp_2}{dr} + \rho\left(c_{\theta,2}\frac{dc_{\theta,2}}{dr} + c_{m,2}\frac{dc_{m,2}}{dr}\right) \tag{3.16}$$

$$\frac{dp_{t,2}}{dr} = \left(\rho\frac{c_{\theta,2}^2}{r} + \rho c_{\theta,2}\frac{dc_{\theta,2}}{dr}\right) + \rho c_{m,2}\frac{dc_{m,2}}{dr} \tag{3.17}$$

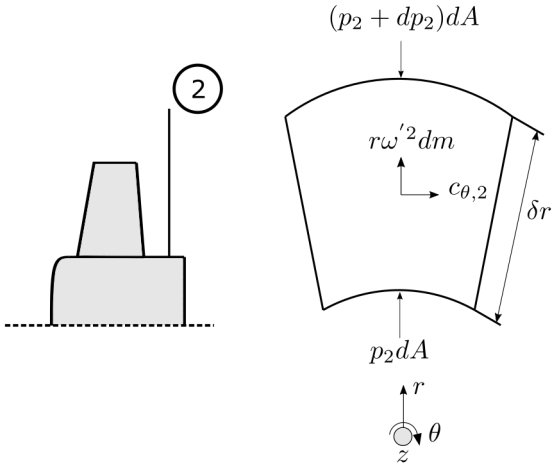

Figure 3.5: Rotor downstream plane (**left**). Forces acting on an elemental mass in the radial direction taken on the rotor downstream plane (**right**), adapted from [31].

$$\frac{1}{\rho}\frac{dp_{t,2}}{dr} = \frac{c_{\theta,2}}{r}\frac{d(rc_{\theta,2})}{dr} + c_{m,2}\frac{dc_{m,2}}{dr} \tag{3.18}$$

Looking at the left-hand side of Eq. (3.18). The total pressure at the rotor downstream plane can be expressed in terms of the specific work done by an elemental blade cascade at a specific radial location according to Eq. (3.19). Here it is assumed that the inlet has no swirl, i.e., assuming zero circumferential velocity component at rotor inlet ($c_{\theta,1} = 0$).

$$Y_{t,CA}(r) = \frac{1}{\rho}(p_{t,2} - p_{t,1}) = \omega r c_{\theta,2} \tag{3.19}$$

Finally differentiating Eq. (3.19) with respect to r and assuming that the total-pressure is not a function of the radius yields Eq. (3.20).

$$\frac{dp_{t,2}}{dr} = \omega\rho\frac{d(rc_{\theta,2})}{dr} \tag{3.20}$$

Combining this with Eq. (3.18), yields Eq. (3.21). Finally, for radial equilibrium to be achieved, i.e., for the streamlines to lie on co-axial cylindrical surfaces Eq. (3.21), needs to be satisfied by every elemental blade cascade along the blade span. The term $rc_{\theta,2}(r)$, is the radial distribution of the swirl and $Y_{t,CA}(r)$ is the loading distribution.

$$\omega\frac{d(rc_{\theta,2})}{dr} = \frac{c_{\theta,2}}{r}\frac{d(rc_{\theta,2})}{dr} + c_{m,2}\frac{dc_{m,2}}{dr} \tag{3.21}$$

During the blade design process, a function is chosen for $rc_{\theta,2}(r)$ to calculate the corresponding unknown $c_{m,2}(r)$. There are two choices for loading distribution available; an iso-energetic loading distribution and radius dependent loading distribution. The blade loading distribution ultimately helps obtain the velocity triangles at the different blade radii.

For an iso-energetic loading distribution, $Y_{t,CA}(r)$ is constant along the blade span. This would reduce Eq. (3.21) down to Eq. (3.22), which will ultimately yield $c_{m,2}$ as a constant along the blade span, i.e., the radial distribution of the meridional velocity at the rotor exit will be uniform and will only depend on the choice of volume flowrate (Q_B) and through-flow area, i.e., area between the blade tip and hub. The meridional velocity at the rotor exit for iso-energetic blade loading distribution is calculated according to Eq. (3.23). Note that, the meridional velocity at the rotor exit is equal to the rotor inlet ($c_{m,1} = c_{m,2}$). Additionally, since a swirl-free inlet is assumed ($c_{\theta,1} = 0$), the absolute velocity at the rotor inlet is also then equal to the meridional velocity at the rotor out, i.e., $c_{m,1} = c_{m,2} = c_1$.

$$c_{m,2}\frac{dc_{m,2}}{dr} = 0 \tag{3.22}$$

$$c_{m,2} = \frac{Q_B}{\pi(r_{tip}^2 - r_{hub}^2)} \tag{3.23}$$

The circumferential velocity at rotor outlet at different radii can be obtained according to Eq. (3.19), where ω is the rotational velocity of the fan and r, is the blade section radius. To achieve a constant value of $rc_{\theta,2}$ along the blade span, for iso-energetic blade loading distribution, the circumferential velocity component at the rotor hub has to be larger compared to at the tip, as radius of the hub is smaller than the tip, i.e, $c_{\theta,hub} > c_{\theta,tip}$. The higher circumferential velocity of the flow at the hub, is achieved through higher flow turning by twisting the blades by a larger angle at the hub compared to the tip. This increases the risk of flow separation at the hub and therefore increases the possibility of significant losses. The remaining parameters of both the inlet and outlet velocity triangles can be obtained using equations presented in Sec. 3.1. A typical distribution of the meridional and circumferential velocity component at the rotor downstream plane is illustrated in Fig. 3.6.

To address the problem of risk of flow separation at the hub using an iso-energetic blade loading distribution, a radius dependent flow loading distribution is often implemented. This approach aims at utilizing higher blade spans more effectively. For a radius dependent blade loading distribution, the specific work done by the elemental blade cascade is a function of the blade radius, and is generalized according to Eq. (3.24), where a and b are constants. Iso-energetic blade loading is a special case of radius dependent blade loading, with $a = 0$. The specific work done per elemental blade cascade is then defined according to Eq. (3.25). Substituting Eq. (3.25) into Eq. (3.21) and integrating over blade section radius (r) yields the meridional velocity component downstream of the rotor. Note that the meridional velocity is no longer

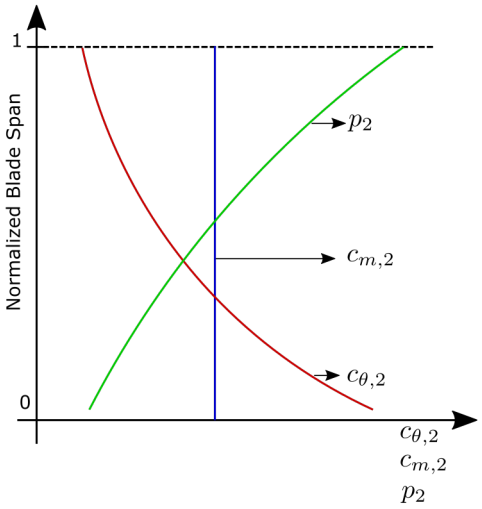

Figure 3.6: Iso-energetic blade loading distribution: Spanwise distribution of $c_{\theta,2}$, p_2, and $c_{m,2}$ downstream to the rotor.

constant along the blade span, and instead is dependent on blade radius.

$$rc_{\theta,2} = ar^n + b \tag{3.24}$$

$$Y_{t,CA} = \omega(ar^n + b) \tag{3.25}$$

$$c_{m,2}(r) = \sqrt{2\left(\omega ar - a^2 log(r) + \frac{ab}{r}\right) + k} \tag{3.26}$$

The remaining steps of determining the velocity triangles at rotor inlet and outlet remain the same as for an iso-energetic blade loading distribution. The only difference being, that the meridional velocity component obtained using Eq. (3.26), must be used to calculate the remainder of the velocity components. Different values of a, b, and k maybe selected to vary the loading along the blade span. However, it must be ensured that blade performance parameters, i.e, $\Delta p_{tt,B}$ and Q_B, is still achieved with the choice of the constants in Eq. (3.26).

Here it is concluded that with the desired volume flowrate, desired total-to-total pressure rise and maximum fan diameter as input and a choice of blade loading distribution and hub diameter, it is possible to determine the inlet and outlet velocity triangles at all blade sections. However, it must be noted that it is assumed here that inlet is swirl free, and all streamlines lie on co-axial cylindrical surfaces due to the radial equilibrium assumption.

3.3 Blade element method

At this stage of the design process, the rotational speed (ω), the fan diameter (d_{fan}), and the density (ρ) are known from the system requirements. The hub diameter (d_{hub}) is assumed such that the hub-to-tip diameter ratio (κ) is below one. The blade count (z_b) is assumed. The assumed choice of blade count and hub diameter is verified later in the design process. The blade loading distribution ($Y_{t,CA}$) is calculated, according to Sec. 3.2, to obtain the inlet and outlet velocity triangles at all blade segments along the blade span.

Here a choice of angle of attack must be made for the chosen airfoil. This is done using the airfoil polar curves for the chosen airfoil. Three options exist for the choice of angle of attack. The first option is to choose the angle of attack (α) such that the peak lift coefficient (C_L) is achieved. This leads to the lowest solidity blades, with maximum blade spacing, which allows for lower manufacturing costs but comes with the disadvantage that the BEP lies close to the stall point and therefore part-load operation becomes important. The second option is to choose the angle of attack (α) such that the minimum drag-to-lift ratio (ε) is achieved which yields blades with maximum hydraulic efficiency. Alternatively, a compromise between the two previous choice may be made.

As an example, from the airfoil polar curves illustrated in Fig. 3.4, for the isolated NACA 4412 airfoil at $Re = 2 * 10^5$, the peak lift coefficient (C_L) of 1.44 is obtained for an angle of attack (α) equal to 15.3°. Similarly, the minimum drag-to-lift ratio (ε) of 0.012 is obtained for an angle of attack of 7°. Either 15.3°, 7°, or an value between the two may be used as the angle of attack of choice for the different blade segments.

With the choice of angle of attack made, all parameters required for the BEM method are now available. The key equation for the BEM method links the blade solidity (σ) to the specific work done by the elemental blade cascade ($Y_{t,CA}$), the velocity triangles, and the aerodynamic airfoil parameters, according to Eq. (3.27). The blade solidity is calculated for all blade segments illustrated in Fig. 3.3.

$$\sigma = \frac{2\ Y_{t,CA}}{w_\infty \omega r\ C_L \left(1 + \frac{\varepsilon}{tan\beta_\infty}\right)} \tag{3.27}$$

The chord length of each blade segment is now calculated. To calculate the blade chord length according to Eq. (3.12), the blade spacing needs to be calculated, according to Eq. (3.28) using the assumed blade count (z_b).

$$s_b = \frac{2\pi r}{z_b} \tag{3.28}$$

Once the chord length (l_c), is calculated for all blade segments, the Reynolds number at all blade segments is calculated according to Eq. (3.29).

$$Re_l = \frac{w_\infty l_c}{\nu} \tag{3.29}$$

Now the choice of blade count (z_b) must be verified. The Reynolds number calculated for each blade segment using the chord length (l_c) using the BEM method, must agree with Reynolds number used to obtain the polar curves for the chosen airfoil. If this criteria is not met, the blade count needs to be changed or a different airfoil polar must be selected until the Reynolds numbers for the airfoil polar matches the one obtained using the chord length as the reference diameter from the BEM method.

Once the blade chord length is determined the twist of the blade along the blade span needs to be calculated, i.e., the stagger angle (γ in Fig. 3.2) for each individual blade segment needs to be determined. The stagger angle of each blade segment is calculated as the sum of the angle of attack (α) and the vectorial mean flow angle (β_∞).

$$\gamma = \beta_\infty + \alpha \tag{3.30}$$

The design of the fan is however only valid between only certain limits. Flow separation is a common concern in fan and compressor design, as the flow experiences an unfavorable pressure gradient as it moves through the blade passage. To check the validity of the design, a few design criteria must be fulfilled by the final design.

The De Haller critierion [44] is commonly employed to limit the flow diffusion within the blade passage. The De Haller number is defined as the ratio of the relative velocity at rotor exit to rotor inlet, according to Eq. (3.31). It is recommended to keep the De Haller number greater than 0.72, at all blade segments. However, this is especially true at the hub, where the maximum flow diffusion is expected. Carolus [15], cites two studies by Marcinowski [45] and Schiller [46], which suggest limiting the flow diffusion at the rotor hub to between $0.55 - 0.60$, for single-stage fans to prevent flow separation at the hub. Additionally, a Diffusion Factor (DF), introduced by Lieblein et al. [47] and calculated according to Eq. (3.32), should be maintained below 0.6 for all blade segments. If the design criteria, is not met at the end of the design process, the initial basic design parameters must be reconsidered.

$$De\ Haller = \frac{w_2}{w_1} \geq 0.72 \tag{3.31}$$

$$DF = \left(1 - \frac{w_2}{w_1}\right) + \left(\frac{w_{\theta,1} - w_{\theta,2}}{2w_1}\right)\left(\frac{s_b}{l_c}\right) \leq 0.6 \tag{3.32}$$

The last step to conclude the blade design process is the stacking of the blade sections in the radial direction. There are several options such as; stacking along the centroid of each individual blade section, stacking along the leading edge, and stacking such that the leading edge forms a sinusoidal curve for acoustic benefits . A holistic optimization study was performed using Evolutionary Algorithms (EA) by Kong et al. [27] and Carolus et al. [26], to optimize the aerodynamic efficiency of low-pressure axial fans by varying the stacking line, and offers a good perspective into the effect of choice of stacking line on aerodynamic performance.

The stacking line may also be varied in three-dimensional space to obtain blade circumferential skew, sweep or dihedral angle [23]. The forward variation of circumferential skew and sweep are commonly implemented methods to improve the aerodynamic efficiency [22, 23, 25–27]. The various choices of stacking line is not explored in this work.

3.4 Geometry summary

The geometry used for both the following appended papers was designed and experimentally tested by Friedrich-Alexander University (FAU) [29, 31]. The summary of the geometry used for all the numerical investigations performed in this work is described here for brevity.

The fan can be described as ducted, rotor-only, low-pressure axial fan. The fan is housed inside a casing, which has three distinct sections; the inlet nozzle, the constant diameter section and the downstream diffusor. The fan is positioned at the geometric center of the constant diameter section, such that it lies midway between the nozzle exit and the diffusor inlet, see Fig. 3.7. The fan has a constant tip-gap of 2.5 mm, and a tip-gap ratio of 2%. Four structural struts are placed on a flange at the end of the diffusor section. The strut and the flange block 8% and 11% of the diffusor exit area respectively. The fan is powered by an external motor, which sits 1.5 casing diameter (d_{casing} in Fig. 3.7) downstream of the diffusor exit.

The fan itself has a hub-to-tip diameter ratio (κ) of 0.5, and nine blades spaced equally in the circumferential direction. The rotor blade uses the NACA 4510 airfoil profile for all blade segments. The NACA 4510 airfoil profile has a maximum camber of 4% the chord length, located at 50%, the chord length. It has a maximum thickness of 10% of the chord length, located at 30.6% of the chord. The blade segments are stacked in the radial direction, such that the centroids of each individual blade segment, lies along the same axial position, see Fig. 3.8. The rotor blade has a span of 123.5 mm.

The rotor blade has an iso-energetic blade loading distribution, i.e., $Y_{t,CA} = 233.3\ m^2/s^2$ is constant along the blade span and the circumferential velocity component at the rotor inlet is assumed to be zero. Since, this is rotor blade has an iso-energetic blade loading distribution, the blade segment at the rotor hub is more twisted than at the tip, see Fig. 3.8. The stagger angle at the hub is 46.3°, and the stagger angle at the tip is 20.7°, leading to a blade twist of 25.6° along the blade span. The angle of attack chosen at the hub and tip are 8° and 10°, respectively.

3.5 Summary

A flowchart is presented in Fig. 3.9 to navigate through the steps outlined in Ch .2 and Ch. 3. In Fig. 3.9, "Check A" refers to a comparison between the Re number obtained from the BEM method, and the Re number used to obtain the polar curves. "Check B", refers to the De Haller number, diffusion factor and blade solidity criteria check outlined in Sec. 3.3.

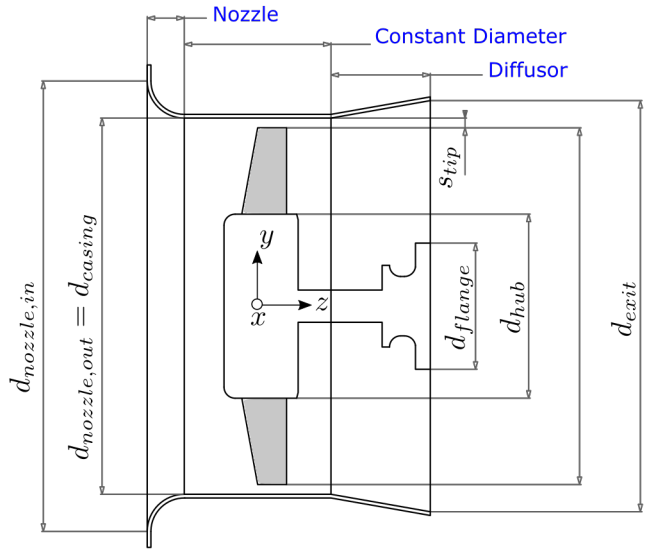

Figure 3.7: Low-pressure axial fan housed inside casing, designed by FAU [29, 31].

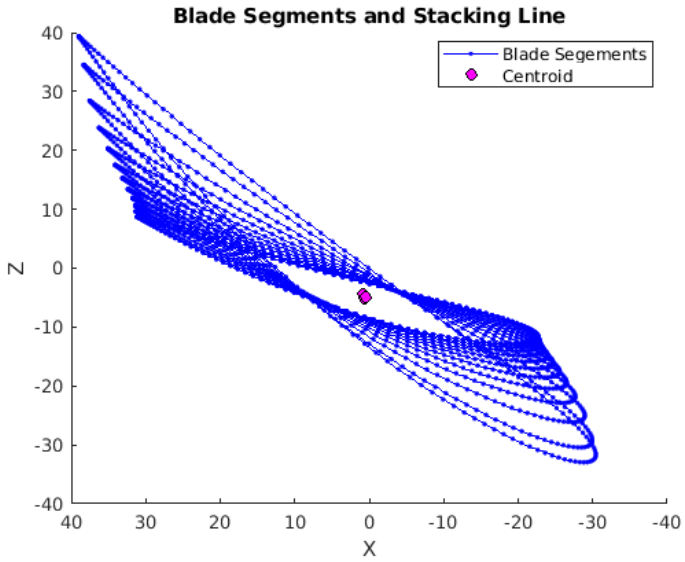

Figure 3.8: Blade sections of NACA 4510 profile stacked along the centroid to generate a low-pressure axial fan, designed by FAU [29, 31].

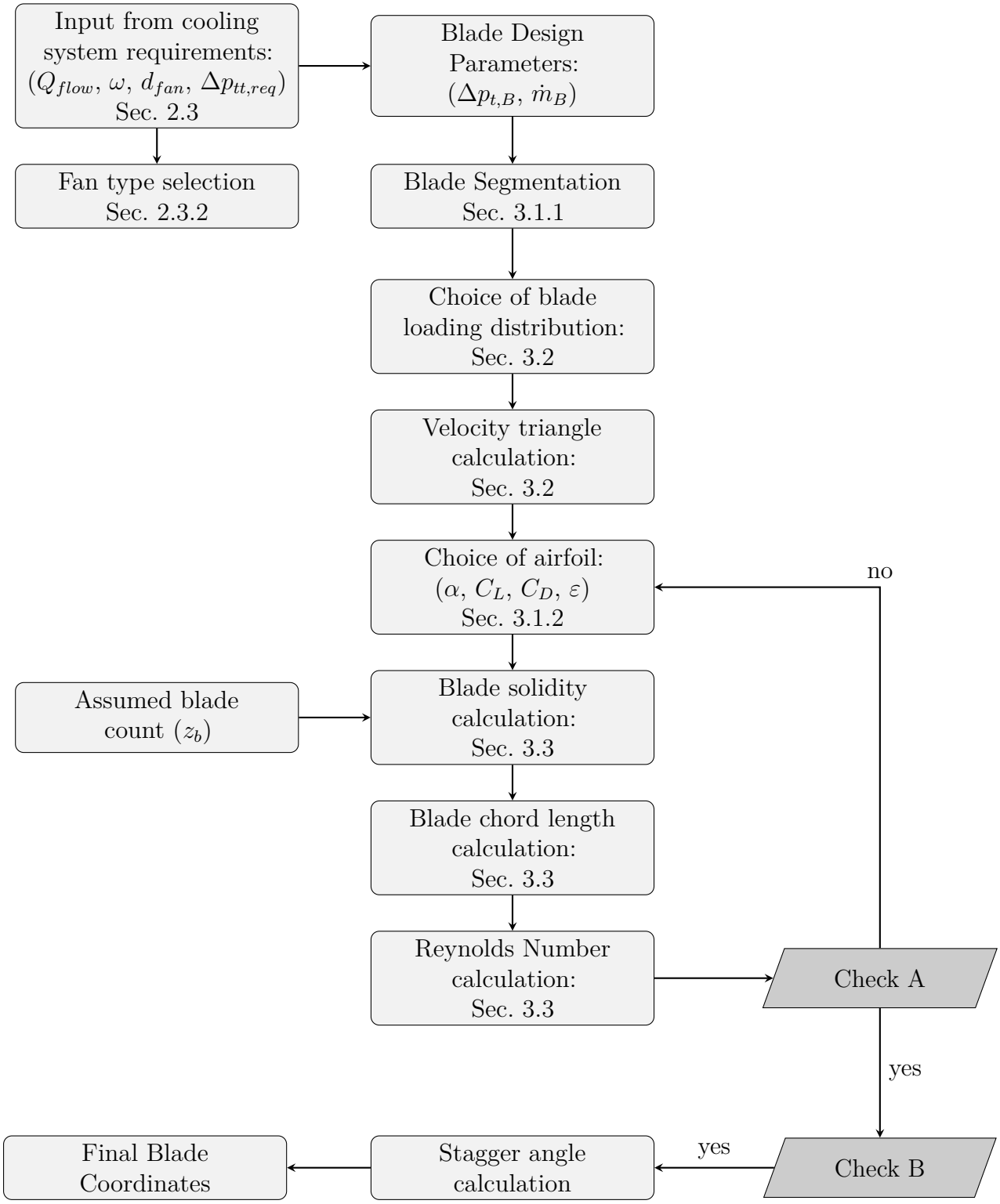

Figure 3.9: Flow chart of blade design process for a low-pressure axial fan using the BEM method.

Chapter 4

Summary of papers

4.1 Paper 1

In Paper 1, the aerodynamic performance a low-pressure axial fan with dimensional resemblance to an automotive cooling fan, was investigated when subjected to an upstream blockage.

4.1.1 Methodology

A ducted rotor-only low-pressure axial fan designed and experimentally tested at Friedrich-Alexander University (FAU) was used for this work [29, 31]. The experimental characteristic curve for a single rotational speed and the three velocity components, i.e., axial, radial and circumferential velocity components at the rotor inlet and outlet was made publicly available by FAU. The geometry of the fan is presented in Sec. 3.4.

The first part of this work focused on the numerical validation of the experimental data from FAU. Three-dimensional, steady state Reynolds-Averaged Navier Stokes (RANS) analysis was performed on a single blade passage for the validation study. The inlet nozzle, the downstream diffusor and the fan-hub cap were included in the Computational Fluid Dynamics (CFD) domain. The structural struts, the hub fillet, and the downstream motor was excluded from the CFD domain, instead the hub was extended to the CFD domain outlet. The choice of turbulence model was investigated. The three commonly used RANS turbulence models, i.e., $k-\varepsilon$, $k-\omega$, and the SST turbulence model were used to simulate the entire characteristic curve for all experimental operating points till the onset of stall. The effect of resolving the boundary layer on the aerodynamic performance was investigated at the experimental BEP. The fan exhausted into a large room, i.e., atmospheric conditions.

Once good agreement was achieved between the numerical and experimental data, the effect of a generic upstream blockage was investigated. A generic blockage in the form of a circular disc was placed upstream to the fan. Three different radial extents of the circular disc was considered, such that the disc blocked 25%, 50% and 75% of the rotor blade span. The axial position of the circular disc upstream to the fan, was maintained at a constant value for all three cases.

4.1.2 Discussion

The validation study yields a good comparison between the numerical data and the experimental data from FAU. Of the three turbulence models used to simulate the characteristic curve, $k-\varepsilon$, was chosen to be the turbulence model of choice. This choice is attributed to the $k-\omega$ and the SST turbulence model exhibiting bi-directional error when compared to the experimental data at overload conditions. Additionally, the $k-\omega$ and the SST turbulence model, predicted an early and sharp onset of stall compared to the experimental data. In comparison, the $k-\varepsilon$ turbulence model, under-predicted both the total-to-total pressure coefficient and the total-to-static efficiency for all experimental data points.

Resolving the boundary layer by implementing wall-y+ values below one provided no significant improvement in the prediction of the aerodynamic performance at the experimental BEP. Therefore, to reduce the computational cost, the boundary layer was modeled using wall-functions by implementing wall-y+ values greater than 11, as recommended by the solver.

A good agreement was achieved between the meridional velocity component at both the rotor inlet and outlet, except at the tip region where RANS models are predictably limited due to the presence of tip vortices. However, a difference was observed in the circumferential velocity component at the rotor inlet. CFD predicted zero circumferential velocity component at the rotor inlet. In comparison, a negative circumferential velocity component, increasing from the blade mid-span to the tip was observed in the experiments. Here it is concluded, that the circumferential velocity component observed in the experiments performed at FAU, was an experimental artifact, possibly a result of the model or rig construction and therefore not predicted by CFD.

The validated numerical setup was used to study the effect of upstream blockage on aerodynamic performance of low-pressure axial fans. The presence of an upstream blockage, predictably led to the formation of a re-circulation region at the rotor hub and flow re-distribution along the blade span. Increasing the radius of the circular disc, led to a decrease in the meridional velocity component at the hub and corresponding a increase at higher blade spans. The aerodynamic performance of the rotor, i.e., the total-to-static pressure and the total-to-static efficiency was observed to decrease significantly with increase in the radius of the circular disc. Additionally, the peak total-to-static efficiency was observed to occur at a lower flow coefficient, with an increase in the flow blockage caused by the upstream circular disc.

4.1.3 Division of work

All numerical investigations were performed by Debarshee Ghosh. Professor Niklas Andersson provided technical supervision for all parts of the work. Associate Professor Sassan Etemad provided project supervision. The geometry and experimental results used in this work were obtained from FAU [29, 31].

4.2 Paper 2

As discussed in Ch. 1, it is a common practice to place multiple cooling fans in parallel as a part of the cooling package, in close proximity to one another. The tightly packed underhood region and heat-exchanger shape limit the fan diameter. In order to circumvent this limitation, multiple cooling fans of small diameters are tightly packaged and placed in parallel. Paper 2 investigates the aerodynamic performance of two low-pressure axial fans installed in parallel.

4.2.1 Methodology

The geometry from FAU used in Paper 1, is used again in this work. Two of these low-pressure axial fans are placed parallel to one another, such that the rotational axes of the two fans are separated by 1.35 times the casing diameter. This is the closest the two fans could be placed to one another without the inlet nozzle of the two fans coming in contact. Axially the two fans are placed in identical axial positions.

First a validation study was performed against the experimental results from FAU, for a single fan. Full annulus, three-dimensional, Unsteady RANS (URANS) analysis with the $k - \varepsilon$ turbulence model was carried out. The motion of the fan was modeled using the sliding mesh approach. The validated numerical setup for a single fan, was then used to investigate the aerodynamic performance of two fans installed in parallel. Both for the single-fan and two-fans in parallel case, only the experimental BEP was investigated numerically, due to the significantly large grid size and small time-step used for the numerical investigations. A correlation study was performed between the pressure signals obtained from the two-fans to identify any coupling of the pressure fields.

4.2.2 Discussion

The validation study performed for a single fan yielded a good comparison with the experimental data from FAU. Minimal differences were observed in the aerodynamic performance parameters compared to experimental data at BEP. An almost identical match was obtained for the meridional velocity component both upstream and downstream of the rotor. A difference was observed in the circumferential component of velocity at the rotor inlet. Similar to the results from Paper 1, CFD predicted zero circumferential velocity along the blade span at the rotor inlet, in comparison to experimental data, which showed an increasing negative circumferential velocity component from the blade mid-span to tip.

The validated numerical setup was then used to investigate the aerodynamic performance for the two fans in parallel. A local diffusion of the flow is observed at the inlet nozzle at the region where the two fans are closest to one another. This local flow diffusion ultimately leads to a circumferential non-uniformity of the flow at the nozzle inlet. The spatial non-uniformity is not identical for the two fans. The non-uniformity also exhibits a temporal variation. The temporal variation of the non-uniformity is minimal but a phase difference was observed across the two

fans. The pressure fields of the two fans exhibit a strong coupling with a maximum correlation observed for a time lag, corresponding to the time taken for the rotor blade to travel half the blade passage. The acceleration of the flow through the nozzle allows the flow to reduce the non-uniformity. Ultimately, no significant difference was observed in the circumferentially and time-averaged velocity components at the rotor inlet. Consequently, only minor differences were observed in the aerodynamic performance of the two fans installed in parallel, both with respect to each other and to a single-fan operating in stand-alone mode.

4.2.3 Division of work

All numerical investigations were performed by Debarshee Ghosh. Professor Niklas Andersson provided technical supervision for all parts of the work. Associate Professor Sassan Etemad provided project supervision. The geometry and experimental results used in this work were obtained from FAU [29, 31].

Chapter 5

Conclusion

5.1 Concluding remarks

The design of low-pressure axial fans using the BEM method, starting from the system-level cooling requirement, has been detailed and will be used in future work to design a low-pressure axial fan with radius-dependent blade loading.

Three-dimensional steady-state RANS simulations were performed for a single blade passage and validated against experimental data from FAU. Similarly, three-dimensional URANS simulations were performed for the full fan annulus and validated against experimental data from FAU. Good agreement with experimental data was achieved both for the single-blade passage and full annulus simulations.

The effect of a generic upstream blockage on the aerodynamic performance of the fan was quantified. It was demonstrated that the increase in radial blockage of the fan inlet predictably led to a substantial drop in aerodynamic performance, early onset of stall, and peak efficiency moving to lower flow coefficients. This illustrates the current issue faced by vehicle manufacturers who buy cooling fans "off the shelf," that have not been designed for conditions specific to those experienced by the fans when installed in an underhood environment. Ultimately leading to fans that perform significantly worse than their specified performance when installed in the underhood region.

The aerodynamic performance of two low pressure axial fans installed in parallel was investigated. Insignificant difference was seen in the aerodynamic performance of the two fans with respect to each other. Additionally, they behaved almost identically to a single fan. This is a positive conclusion for vehicle manufacturers using multiple fans in parallel.

5.2 Future work

All numerical investigations performed up until now used the geometry and experimental results obtained from FAU [29, 31]. However, limitations arose due to the lack of control over the fan design and experimental setup. To overcome these limitations, designing a new fan with a radius-dependent blade loading distribution is recommended. An experimental investigation using Laser Doppler Anemometry (LDA) to obtain aerodynamic characteristic curves and velocity components to validate the new fan design is recommended. Furthermore, multi-objective optimization studies using evolutionary algorithms and meta-models on the new fan design subjected to non-uniform inlet conditions are suggested to mimic underhood inflow conditions. The non-uniform flow conditions can be obtained from CFD simulations of a generic underhood region.

To better understand the behavior of low-pressure axial fans when installed in parallel, it is recommended to explore more relevant industrial scenarios. It is worth noting that the fans currently used for automotive cooling typically do not have an inlet nozzle, to ensure tighter packaging. This allows for the fans to be placed almost in contact with one another, which differs from the case studied in Paper 2, where fans had to be spaced further apart due to the inlet nozzle. Additionally, the lack of a nozzle means that any flow non-uniformity is directly ingested by the fan, which may impact performance. As a result, future research should investigate the effects of removing the inlet nozzle, varying the horizontal spacing between fans, and the use of counter-rotating fans on aerodynamic performance.

Bibliography

[1] *Paris Agreement*. URL: https://treaties.un.org/pages/ViewDetails.aspx?src=TREATY&mtdsg_no=XXVII-7-d&chapter=27&clang=_en (visited on 03/28/2019) (cit. on p. 3).

[2] *Global EV Outlook 2022 – Analysis*. 2022. URL: https://www.iea.org/reports/global-ev-outlook-2022 (cit. on p. 3).

[3] Ahmad A Pesaran. "Battery thermal models for hybrid vehicle simulations". In: *Journal of power sources* 110.2 (2002), pp. 377–382 (cit. on p. 4).

[4] Matthew Zolot, Ahmad A Pesaran, and Mark Mihalic. "Thermal evaluation of Toyota Prius battery pack". In: *SAE technical paper* (2002), pp. 01–1962 (cit. on pp. 4, 6).

[5] M D Zolot, K Kelly, M Keyser, M Mihalic, A Pesaran, and A Hieronymus. "Thermal Evaluation of the Honda Insight Battery Pack: Preprint". In: () (cit. on pp. 4, 6).

[6] K.J. Kelly, M. Mihalic, and M. Zolot. "Battery usage and thermal performance of the Toyota Prius and Honda Insight during chassis dynamometer testing". In: *Seventeenth Annual Battery Conference on Applications and Advances. Proceedings of Conference (Cat. No.02TH8576)*. 2002, pp. 247–252. DOI: 10.1109/BCAA.2002.986408 (cit. on pp. 4, 6).

[7] ÁG Miranda and CW Hong. "Integrated modeling for the cyclic behavior of high power Li-ion batteries under extended operating conditions". In: *Applied energy* 111 (2013), pp. 681–689 (cit. on p. 4).

[8] Yonghuang Ye, Yixiang Shi, and Andrew AO Tay. "Electro-thermal cycle life model for lithium iron phosphate battery". In: *Journal of Power Sources* 217 (2012), pp. 509–518 (cit. on p. 4).

[9] Riza Kizilel, Rami Sabbah, J Robert Selman, and Said Al-Hallaj. "An alternative cooling system to enhance the safety of Li-ion battery packs". In: *Journal of Power Sources* 194.2 (2009), pp. 1105–1112 (cit. on p. 4).

[10] Zhonghao Rao, Shuangfeng Wang, Maochun Wu, Zirong Lin, and Fuhuo Li. "Experimental investigation on thermal management of electric vehicle battery with heat pipe". In: *Energy Conversion and Management* 65 (2013), pp. 92–97 (cit. on p. 4).

[11] Thanh-Ha Tran, Souad Harmand, and Bernard Sahut. "Experimental investigation on heat pipe cooling for hybrid electric vehicle and electric vehicle lithium-ion battery". In: *Journal of power sources* 265 (2014), pp. 262–272 (cit. on p. 4).

[12] Ahmad A Pesaran. "Battery thermal management in EV and HEVs: issues and solutions". In: *Battery Man* 43.5 (2001), pp. 34–49 (cit. on pp. 4, 6).

[13] Kim Yeow, Ho Teng, Marina Thelliez, and Eugene Tan. "Comparative study on thermal behavior of lithium-ion battery systems with indirect air cooling and indirect liquid cooling". In: *International Symposium on Flexible Automation*. Vol. 45110. American Society of Mechanical Engineers. 2012, pp. 585–591 (cit. on pp. 5, 6).

[14] Dafen Chen, Jiuchun Jiang, Gi-Heon Kim, Chuanbo Yang, and Ahmad Pesaran. "Comparison of different cooling methods for lithium ion battery cells". In: *Applied Thermal Engineering* 94 (2016), pp. 846–854 (cit. on p. 6).

[15] T. Carolus. *Fans: Aerodynamic Design, Noise Reduction, Optimization*. Springer: Berlin/Heidelberg, Germany, 2022. ISBN: 978-3-658-37958-2 (cit. on pp. 7, 13, 14, 16, 17, 20, 22, 23, 29).

[16] B.E. S. Larry Dixon and C. Hall. *Fluid Mechanics and Thermodynamics of Turbomachinery*. Elsevier Science, 2013. ISBN: 9780124159549 (cit. on pp. 7, 13, 20).

[17] Stefano Castegnaro. "Aerodynamic design of low-speed axial-flow fans: a historical overview". In: *Designs* 2.3 (2018), p. 20 (cit. on p. 7).

[18] R Allan Wallis. *Axial Flow Fans: design and practice*. Academic Press, 2014 (cit. on p. 7).

[19] Thomas H Carolus and Ralf Starzmann. "An aerodynamic design methodology for low pressure axial fans with integrated airfoil polar prediction". In: *Turbo Expo: Power for Land, Sea, and Air*. Vol. 54648. 2011, pp. 335–342 (cit. on pp. 7, 23).

[20] R.J. Downie, M.C. Thompson, and R.A. Wallis. "An engineering approach to blade designs for low to medium pressure rise rotor-only axial fans". In: *Experimental Thermal and Fluid Science* 6.4 (1993), pp. 376–401. ISSN: 0894-1777. DOI: https://doi.org/10.1016/0894-1777(93)90016-C (cit. on p. 7).

[21] Ja´ nos Vad and Csaba Horva´ th. "The impact of the vortex design method on the stall behavior of axial flow fan and compressor rotors". In: *Turbo Expo: Power for Land, Sea, and Air*. Vol. 43161. 2008, pp. 229–238 (cit. on p. 8).

[22] M. G. Beiler and T. H. Carolus. "Computation and Measurement of the Flow in Axial Flow Fans With Skewed Blades". In: *Journal of Turbomachinery* 121.1 (Jan. 1999), pp. 59–66. ISSN: 0889-504X. DOI: 10.1115/1.2841234. eprint: https://asmedigitalcollection.asme.org/turbomachinery/article-pdf/121/1/59/5725321/59_1.pdf (cit. on pp. 8, 30).

[23] Jie Wang and Niels P Kruyt. "Effects of sweep, dihedral and skew on aerodynamic performance of low-pressure axial fans with small hub-to-tip diameter ratio". In: *Journal of Fluids Engineering* 144.1 (2022) (cit. on pp. 8, 23, 30).

[24] Massimo Masi, Manuel Piva, and Andrea Lazzaretto. "Design guidelines to increase the performance of a rotor-only axial fan with constant-swirl blading". In: *Turbo Expo: Power for Land, Sea, and Air*. Vol. 45578. American Society of Mechanical Engineers. 2014, V01AT10A033 (cit. on pp. 8, 23).

[25] J Vad, A. R A. Kwedikha, Cs Horváth, M Balczó, M. M. Lohász, and T Régert. "Aerodynamic effects of forward blade skew in axial flow rotors of controlled vortex design". In: *Proceedings of the Institution of Mechanical Engineers, Part A: Journal of Power and Energy* 221.7 (2007), pp. 1011–1023. DOI: 10.1243/09576509JPE420. eprint: https://doi.org/10.1243/09576509JPE420 (cit. on pp. 8, 30).

[26] Thomas Carolus and Konrad Bamberger. "Axial Impeller-Only Fans with Optimal Hub-to-Tip Ratio and Blades Adapted for Minimum Exit Loss". In: *International Journal of Turbomachinery, Propulsion and Power* 8.1 (2023). ISSN: 2504-186X (cit. on pp. 8, 23, 29, 30).

[27] Chuang Kong, Meng Wang, Tao Jin, and Shaoliang Liu. "An optimization on the stacking line of low-pressure axial-flow fan using the surrogate-assistant optimization method". In: *Journal of Mechanical Science and Technology* 35 (2021), pp. 4997–5005 (cit. on pp. 8, 29, 30).

[28] Jie Wang and Niels P. Kruyt. "Computational Fluid Dynamics Simulations of Aerodynamic Performance of Low-Pressure Axial Fans With Small Hub-to-Tip Diameter Ratio". In: *Journal of Fluids Engineering* 142.9 (May 2020). 091202. ISSN: 0098-2202. DOI: 10.1115/1.4047120. eprint: https://asmedigitalcoll\-ection.asme.org/fluidsengineering/article-pdf/142/9/091202/6537190/fe_142_09_091202.pdf (cit. on pp. 8, 23).

[29] Florian Zenger, Clemens Junger, Manfred Kaltenbacher, and Stefan Becker. *A benchmark case for aerodynamics and aeroacoustics of a low pressure axial fan*. Tech. rep. SAE Technical Paper, 2016 (cit. on pp. 8, 30, 31, 33, 34, 36, 38).

[30] Florian Zenger, Gert Herold, and Stefan Becker. "Acoustic Characterization of Forward- and Backward-Skewed Axial Fans Under Increased Inflow Turbulence". In: *AIAA Journal* 55.4 (2017), pp. 1241–1250. DOI: 10.2514/1.J055383. eprint: https://doi.org/10.2514/1.J055383 (cit. on p. 8).

[31] Florian J. Krömer. "Sound emission of low-pressure axial fans under distorted inflow conditions". doctoralthesis. FAU University Press, 2018, XVIII, 253 S. DOI: 10.25593/978-3-96147-089-1 (cit. on pp. 8, 25, 30, 31, 33, 34, 36, 38).

[32] Stefan Schoder, Clemens Junger, and Manfred Kaltenbacher. "Computational aeroacoustics of the EAA benchmark case of an axial fan". In: *Acta Acustica* 4.5 (2020), p. 22 (cit. on p. 8).

[33] Tao Zhu and Thomas H Carolus. "Experimental and numerical investigation of the tip clearance noise of an axial fan". In: *Turbo Expo: Power for Land, Sea, and Air*. Vol. 55188. American Society of Mechanical Engineers. 2013, V004T10A001 (cit. on p. 8).

[34] G Y Jin, H Ouyang, Y D Wu, and Z H Du. "Experimental and numerical investigations of the tip leakage flow of axial fans with circumferential skewed blades under off-design conditions". In: *Proceedings of the Institution of Mechanical Engineers, Part C: Journal of Mechanical Engineering Science* 224.6 (2010), pp. 1203–1216. DOI: 10.1243/09544062JMES1813. eprint: https://doi.org/10.1243/09544062JMES1813 (cit. on p. 8).

[35] Yonggang Gou, Xiuzhi Shi, Jian Zhou, Xianyang Qiu, and Xin Chen. "Characterization and effects of the shock losses in a parallel fan station in the underground mine". In: *Energies* 10.6 (2017), p. 785 (cit. on p. 8).

[36] Juan P Hurtado and EI Acuña. "CFD analysis of 58 Adit main fans parallel installation for the 2015–2019 underground developments of the new level mine project". In: *Applied Thermal Engineering* 90 (2015), pp. 1109–1118 (cit. on p. 8).

[37] Sandra Velarde Suárez, F Israel Guerras Colón, José González, Katia M Argüelles Díaz, Jesús M Fernández Oro, Carlos Santolaria-Morros, and Juan Bernal-Cantón. "Evaluation of Interaction and Blockage Effects for Multi-fan Units used in Public Transport HVAC Systems". In: *International Journal of Ventilation* 13.4 (2015), pp. 339–350 (cit. on p. 8).

[38] Peter F. Pelz and Stefan S. Stonjek. "The Influence of Reynolds Number and Roughness on the Efficiency of Axial and Centrifugal Fans—A Physically Based Scaling Method". In: *Journal of Engineering for Gas Turbines and Power* 135.5 (Apr. 2013). 052601. ISSN: 0742-4795. DOI: 10.1115/1.4022991. eprint: https://asmedigitalcollection.asme.org/gasturbinespower/article-pdf/135/5/052601/6157539/gtp_135_5_052601.pdf (cit. on p. 13).

[39] Nicola Aldi, Nicola Casari, Michele Pinelli, and Alessio Suman. "A statistical survey on the actual state-of-the-art performance of radial flow fans based on market data". In: *Proceedings of FAN 2018 Conference*. 2018, pp. 18–20 (cit. on p. 13).

[40] Isaak E Idelchik. "Handbook of hydraulic resistance". In: *Washington* (1986) (cit. on p. 14).

[41] Otto Cordier. "Ähnlichkeitsbedingungen für Strömungsmaschinen". In: *BWK Bd* 6.10 (1953) (cit. on p. 16).

[42] Ira H Abbott and Albert E Von Doenhoff. *Theory of wing sections: including a summary of airfoil data*. Courier Corporation, 2012 (cit. on p. 23).

[43] Mark Drela. "XFOIL: An analysis and design system for low Reynolds number airfoils". In: *Low Reynolds Number Aerodynamics: Proceedings of the Conference Notre Dame, Indiana, USA, 5–7 June 1989*. Springer. 1989, pp. 1–12 (cit. on p. 23).

[44] P De Haller. “Das verhalten von tragflügelgittern in axialverdichtern und im windkanal”. In: *Brennstoff-Wärme-Kraft (BWK)* 5.333 (1953), p. 24 (cit. on p. 29).

[45] Heinz Marcinowski. “" Optimalprobleme bei Axialventilatoren”. PhD thesis. Technischen Hochsehule, 1956 (cit. on p. 29).

[46] Frank Schiller. “Theoretical and experimental studies to determine the load limit for highly loaded axial fans”. PhD thesis. Technical University of Braunschweig, 1984 (cit. on p. 29).

[47] Seymour Lieblein, Francis C Schwenk, and Robert L Broderick. *Diffusion factor for estimating losses and limiting blade loadings in axial-flow-compressor blade elements*. Tech. rep. National Advisory Committee For Aeronautics Cleveland OH Lewis Flight ..., 1953 (cit. on p. 29).